

**SINTERING AND DENSIFICATION BEHAVIOR
OF GDC INFILTRATED POROUS
GDC ELECTROLYTE**

A Thesis Submitted to
the Graduate School of
İzmir Institute of Technology
in Partial Fulfillment of the Requirements for the Degree of
MASTER OF SCIENCE
in Energy Engineering

by
Sinem TEKİN

July 2021
İZMİR

ACKNOWLEDGMENTS

In the beginning, I would like to my advisor Prof. Dr. Sedat Akkurt for his guidance, comments, suggestions, and support. I am also very grateful to my co-advisor, Assist. Prof. Dr. Özgenç Ebil for his scientific advice and insightful discussions. I also would like to thank to members of the thesis committee, Prof. Dr. Muhsin Çiftçioğlu and Assist. Prof. Dr. Mehmet Faruk Ebeoğlugil for their valuable and guiding comments and suggestions. I am thankful for IYTE MAM members, Burcu Akdağ Çağlar, Mutlu Devran Yaman, Duygu Oğuz Kılıç, İşin Özçelik, Zehra Sinem Yılmaz for their technical assistance. Also during this time, I would like to thank Dr. Can Sındıracı, Muhammet Şakir Abdullah Eren, Seda Çakırlar.

I wish to thank all my family especially to my mother Hediye Tekin, friends, and my managers for their supports.

I dedicate this thesis to the memory of my grandmother Medine Tekin.

ABSTRACT

SINTERING AND DENSIFICATION BEHAVIOR OF GDC INFILTRATED POROUS GDC ELECTROLYTE

It is desired that the electrolytes used in solid oxide fuel cells have a dense structure. Ceria-based electrolytes require temperatures of 1400-1500°C to densify. High densification temperatures make this material less in demand despite its good ionic conductivity. In this study, it was aimed to sinter and densify porous GDC scaffolds made of GDC ($\text{Gd}_{0.10}\text{Ce}_{0.90}\text{O}_{1.95}$) material at low temperatures using infiltration technique. A porous GDC scaffold is first produced by sintering the GDC pellet around 1000°C to obtain an intermediate product ready to be infiltrated by a GDC-bearing solution. Multiple infiltration and drying cycles were intended to fill the pores by GDC nanoparticles which are expected to densify at lower temperatures. Two different groups (infiltrated and non-infiltrated) were formed and their densification behaviors with temperature and infiltration repetition cycles were investigated using a vertical dilatometer. The porous GDC scaffold was infiltrated with a polymeric solution prepared from $\text{Ce}(\text{NO}_3)_{3.6}\text{H}_2\text{O}$ and $\text{Gd}(\text{NO}_3)_{3.6}\text{H}_2\text{O}$. The prepared samples were sintered at 1400°C. As a result of the experiments, it was observed that the densification decreased with the increase in temperature and infiltration cycles. This is thought to be because the porous scaffold could not be completely dried during the infiltration cycles. This led to the formation of a dense outer layer of GDC and porous inner layer. This dense layer inhibited shrinkage of the pellet during dilatometric analysis. Further studies need to be conducted to fully evaporate the solvent during drying of the infiltrated pellets.

Keywords and Phrases: Fuel Cell, SOFC, Elecrolyte, Sintering, Densification

ÖZET

GDC İNFİLTRE EDİLMİŞ GÖZENEKLİ GDC ELEKTROLİTİNİN SİNTERLEME VE YOĞUNLAŞMA DAVRANIŞI

Katı oksit yakıt pillerde kullanılan elektrolitlerin yoğun bir yapıya sahip olması istenir. Ceria bazlı elektrolitler yoğunlaşmak için 1400-1500°C gibi sıcaklıklara ihtiyaç duyar. Yüksek yoğunlaşma sıcaklıklarını iyi bir iyonik iletkenliğe sahip olmasına rağmen bu malzemin daha az talep görmesine neden olur. Bu çalışmada GDC ($\text{Gd}_{0.10}\text{Ce}_{0.90}\text{O}_{1.95}$) malzemesinden üretilmiş gözenekli GDC yapı iskelelerinin düşük sıcaklıklarda infiltrasyon destekli sinterleme tekniği ile sinterlenmesi ve yoğunlaştırılması amaçlanmıştır. Gözenekli bir GDC iskelesi, önce GDC taşıyan bir çözelti tarafından infiltreye hazır bir ara ürün elde etmek için GDC peletinin 1000°C civarında sinterlenmesiyle üretilir. Çoklu infiltrasyon ve kurutma döngülerinin, gözenekleri daha düşük sıcaklıklarda yoğunlaşması beklenen GDC nanoparçacıkları ile doldurması amaçlandı. İki farklı grup oluşturulmuş (infiltre edilmiş ve infiltre edilmemiş) ve dikey dilatometre kullanılarak sıcaklık ve infiltrasyon tekrarlama döngüleri ile yoğunlaşma davranışları incelenmiştir. Gözenekli GDC iskelesi, CeO_2 ve Gd_2O_3 tuzlarından hazırlanan polimerik bir çözelti ile infiltre edildi. Hazırlanan numuneler 1400°C'de sinterlenmiştir. Deneyler sonucunda sıcaklık ve infiltrasyon döngülerinin artmasıyla yoğunlaşmanın azlığı gözlemlenmiştir. Bunun nedeninin, infiltre döngüleri sırasında gözenekli yapı iskelesinin tamamen kurutulamaması olduğu düşünülmektedir. Bu, yoğun bir dış GDC tabakasının ve gözenekli iç tabakanın oluşumuna yol açtı. Bu yoğun tabaka, dilatometrik analiz sırasında peletin büzülmesini engelledi. İnfiltre edilen peletlerin kurutulması sırasında çözücünün tamamen buharlaşması için daha ileri çalışmaların yapılması gerekmektedir.

Anahtar Kelimeler ve Deyimler: Yakıt Hücreleri, KOYH, Elektrolit, Sizma, Sinterleme, Yoğunlaştırma

TABLE OF CONTENTS

LIST OF FIGURES	vii
LIST OF TABLES.....	ix
CHAPTER 1. INTRODUCTION	1
1.1. Fuel Cells.....	1
1.2. Types of fuel cells	3
1.3. Working Principle of Fuel Cells.....	5
1.4. Why is Hydrogen Preferred?.....	8
1.5. Components of SOFC.....	8
1.5.1. Anode.....	9
1.5.2. Cathode.....	11
1.5.3. Electrolyte.....	12
1.6. Sintering and Densification in Ceramic Materials	13
1.6.1. Sintering Process	15
1.6.2. Solid State Sintering	17
1.7. Thermal Expansion Measurement with Dilatometer.....	20
1.7.1. Working Principle of the Dilatometer	21
CHAPTER 2. EXPERIMENTAL METHODS	25
2.1. Fabrication of Porous GDC Scaffold Electrolyte	27
2.1.1. Preparation of Pellets.....	27
2.1.2. Polymeric Precursor Solution Preparation	28
2.1.3. Dilatometric Analysis of non-Infiltrated GDC Pellets (Group A samples).....	28
2.1.4. Creation of Porous Scaffolds from Infiltrated GDC Pellets (Group B Samples).....	29
2.1.5. Infiltration Process.....	30
2.1.6. Weight and Density Measurements	31
2.1.7. Structural and Microstructural Characterization	33
CHAPTER 3. RESULTS AND DISCUSSION.....	34
3.1. SEM Analyses	34
3.2. XRD and EDX Analysis Results.....	37
3.3. Dilatometric Analyses	38
CHAPTER 4. CONCLUSION	47

REFERENCES	49
------------------	----

LIST OF FIGURES

<u>Figure</u>	<u>Page</u>
Figure 1. 1. The amount of energy the world produced from energy resources by years.	1
Figure 1. 2. Systematic view of a typical fuel cell.....	2
Figure 1. 3. Classification types of fuel cells.....	5
Figure 1. 4. Scheme and performance of a SOFC and SOFC stack operating with different.....	6
Figure 1. 5. Components that constitute a singular solid cell.....	9
Figure 1. 6. An anode reaction scheme using H ₂ as fuel.	10
Figure 1. 7. Schematic diagram of a cathode-electrolyte interface showing the formation of a triple phase boundary (TPB).	11
Figure 1. 8. The stages of neck formation of two powder particles by sintering and the combination of powders to become a single powder with a diameter of 1.26.....	15
Figure 1. 9. Sintering mechanisms and dependence of the dominant mechanism on the sintering temperature.	16
Figure 1. 10. A representation of the transport of mass from a convex to a concave surface.....	18
Figure 1. 11. A demonstration of the sintering mechanism.....	18
Figure 1. 12. Densification curves (A) and Shrinkage velocity curves (B) of Ce _{0.8} Gd _{0.2} O _{1.9} are given.....	20
Figure 1. 13. Schematic representation of a dilatometer device.....	21
Figure 1. 14. a) Leakage of solution into the porous structure. b) Formation of an interparticle film layer after infiltration.	24
Figure 2. 1. Schematic representation of the experimental steps followed in this thesis.	26
Figure 2. 2. a) Steel mold used to prepare 5mm long pellets. b) and c) view from different angles of the dimensions of pelletized GDC powders.	27
Figure 2. 3. a) Box furnace used for sintering GDC pellets which were sintered at 1000°C to form the porous scaffold. b) The GDC porous scaffold.	29

<u>Figure</u>	<u>Page</u>
Figure 2. 4. Simple demonstration of infiltration of air pockets within a semi-fired scaffold.....	30
Figure 2. 5. a) Immersion of the porous GDC scaffold into the precursor liquid. b) Filling the inside of the pores with liquid by vacuuming. c) Removing the solution and other organics from the pellets.	31
Figure 2. 6. Measuring weight with Archimedes method.....	32
Figure 3. 1. SEM image of the untreated as-received green GDC powder. Agglomerate formations are observed in the sample.....	35
Figure 3. 2. a) Porous GDC pellet sintered at 1000°C and b) SEM image of this pellet.35	
Figure 3. 3. SEM images of fracture surfaces of sintered samples. a) GDC-A1 sample after 1250°C heat treatment. b) Sample GDC-A2 after heat treatment at 1400°C. c) GDC-B3 after sintering at 1400°C. d) GDC-B4 after sintering at 1400°C.....	36
Figure 3. 4. XRD pattern of the prepared GDC powders. CuK α radiation was used. All peaks corresponded to GDC	37
Figure 3. 5. Energy dispersive X-Ray spectroscopy (EDX) analyses of GDC.	38
Figure 3. 6. Relative density and densification rate as a function of temperature a) GDC-A1 b) GDC-A2 c) GDC-B3 and d) GDC-B4.....	39
Figure 3. 7. The variation of the linear shrinkage behavior of the GDC samples with temperature. a) GDC-A1, b) GDC-A2, c) GDC-B3 and d) GDC-B4.....	41
Figure 3. 8. Relative shrinkage curves of infiltrated and non-infiltrated GDC pellets sintered at 1400°C in different cycles.	42
Figure 3. 9. Shrinkage rate curves of infiltrated and non-infiltrated GDC pellets sintered at 1400°C in different cycles.....	42
Figure 3. 10. Demonstration of particle growth in the porous structure of nano GDC powder at room temperature and nano GDC powders fired at 800-900°C..	43
Figure 3. 11. a) Inner surface b) outer surface of infiltrated porous scaffold.....	45
Figure 3. 12. a) The pellet used by Sındırac et al., b) the pellet used in this study.	45
Figure 3. 13. a) Matt interior b) glossy exterior of infiltrated porous scaffold.....	46

LIST OF TABLES

<u>Table</u>	<u>Page</u>
Table 1. 1. Classification of fuel cells according to the electrolyte used and operating temperatures	3
Table 2. 1. Group A non-infiltrated GDC sample codes.	28
Table 2. 2. Group B infiltrated sample codes.	29
Table 3. 1. Elemental composition as atomic percent and weight percent of GDC powder was determined by semi-quantitative EDS analysis.	38
Table 3. 2. Sintering temperatures and final densities of samples.....	40

CHAPTER 1

INTRODUCTION

1.1. Fuel Cells

Energy is the ability of an object or system to do work. The need for energy, which has been an indispensable part of human life from past to present, is increasing day by day. There are many types of energy. Some of them are electricity, heat, magnetic, nuclear, chemical, mechanical, etc. Increasing world population, developing technology and industry have brought along an increase in the amount of energy needed (Figure 1.1). Energy plays a significant role in the social and economic development and progress of countries and in determining policies between countries (Machrafi 2012).

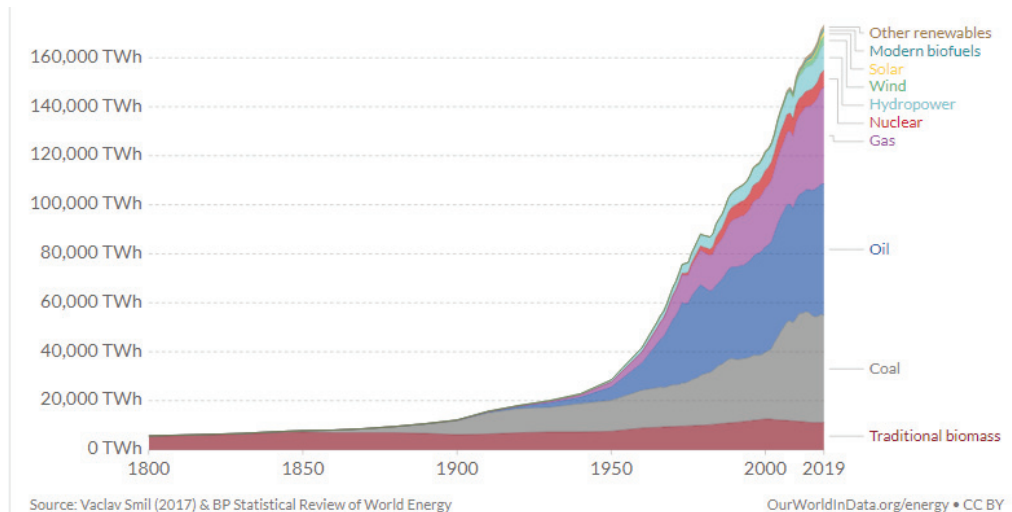


Figure 1. 1. The amount of energy the world produced from energy resources by years.

(Source: <https://ourworldindata.org/grapher/global-energy-substitution?time=earliest..latest>)

Energy is obtained from various sources. Essentially these sources are divided into two. The first of these is the energy obtained from fossil-based fuels (coal, oil, natural gas, etc.), the second is the energy obtained from renewable energy sources (Viswanathan 2016).

The limitations of fossil-based fuels, their damages to the environment (global warming, climate change, greenhouse gas emissions, etc.) and the 1973 oil crisis led to the development of new and renewable energy sources. Renewable energy sources are solar, wind, hydropower, geothermal, biomass and hydrogen energy sources (Viswanathan 2016). In addition to these energy research studies have been carried out in many different fields. During these researches, new and improvable fuel cell technology has attracted a lot of attention.

A fuel cell is an electrochemical cell that converts chemical energy into electrical energy without burning. Since there is no combustion, no gas emissions occur (Hoogers 2002). This makes them more environment friendly than other energy sources. The designs of fuel cells are, quite simple and the variation of the fuel used is high (Figure 1.2.) (Minh and Takahashi, 1995).

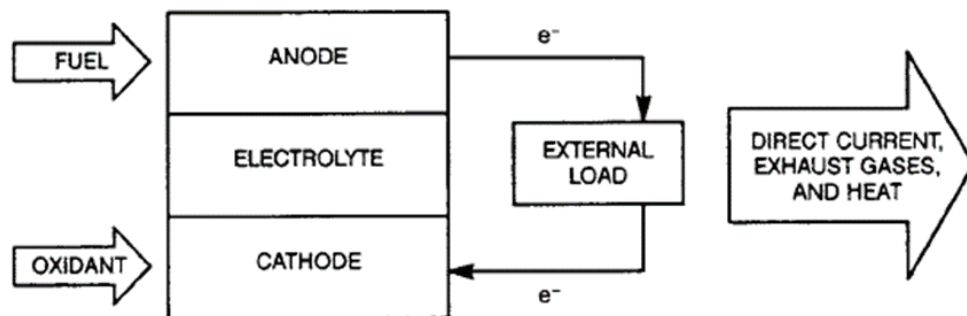


Figure 1. 2. Systematic view of a typical fuel cell.

(Source: Minh and Takahashi 1995).

Moreover, fuel cells; It has many advantages such as high energy efficiency, quiet operation, direct energy conversion, modularity, no polluting emissions, heat recovery and dimensional flexibility (M. Kaur, Kaur, and Kumar 2020). As a result fuel cells are

considered to be a promising, reliable and environmentally friendly energy source (Sındırıcı et al. 2019).

1.2. Types of fuel cells

The fuel cell consists of an anode, a cathode and an electrolyte. There are different types of fuel cells. Generally, fuel cells are classified according to the electrolyte used and operating temperatures (Sundén 2019). The fuel cells are given in the following Table 1.1. according to the electrolyte used and operating temperatures.

Table 1. 1. Classification of fuel cells according to the electrolyte used and operating temperatures.

Fuel Cell	Electrolyte Used	Operation Temperature (°C)	Efficiency %	Application
PEM (Polymer Electrolyte Membrane Fuel Cell)	Polymer Membrane	60-110	40-50	Portable, Mobile, Low power generation.
AFC (Alkaline Fuel Cell)	Potassium Hydroxide	70-130	50-60	Mobile, space, military.
PAFC (Phosphoric Acid Fuel Cell)	Phosphoric Acid	175-210	40-50	Medium to large scale power generation and CHP (Combined Heat and Power).
MCFC (Molten Carbonate Fuel Cell)	Lithium/Potassium Carbonate	550-650	50-60	Large scale power generation.
SOFC (Solid Oxide Fuel Cell)	Ceramics, e.g., YSZ	500-1000	40-72	Vehicle auxiliary power units, medium to large scale power generation and CHP, off-grid power and micro CHP.
DMFC (Direct Methanol Fuel Cell)	Polymer Membrane	70-130	20-50	Mobile, portable.

Like many devices, fuel cells have advantages and disadvantages. For example;

Polymer electrolyte membrane (PEM) fuel cells (also called proton exchange membrane fuel cells) have the advantage of lower weight and volume compared to other

fuel cells (Sundén 2019). In PEM fuel cells, are solid polymer and a platinum (or platinum alloy-containing catalyst) electrode used as the electrolyte. They are cells that operate at low temperatures, so cell components wear less and last longer (Mench 2006). One of them main disadvantages of this cell type is the catalyst costs used. In addition to platinum catalyst is exceptionally susceptible to carbon monoxide poisoning (Sundén 2019).

Alkaline fuel cells (AFCs) are one of the first fuel cell technologies developed. It has been widely used in the US space program to generate electric power and water on a spacecraft (Giorgi 2013). These fuel cells use a solution of potassium hydroxide in water as the electrolyte. It can use a variety of non-precious metals as a catalysts. The most important challenge for AFCs is that they are susceptible to carbon dioxide (CO_2) poisoning. However, the fluid suffers from electrolyte management and electrolyte degradation issues (Mench 2006) .

Phosphoric acid fuel cells (PAFCs) use liquid phosphoric acid as the electrolyte. This cell type is highly resistant to carbon monoxide poisoning. However, it tends to have a lower efficiency than other types of fuel cells in generating electricity (Sundén 2019).

Molten carbonate fuel cells (MCFCs) use a liquid solution of alkali carbonate salts as the electrolyte (Giorgi and Leccese 2013). This cell type works at high temperatures. If MCFCs are used with combined cycle heat systems, their efficiency increases. But; the high operating temperature causes corrosion in the electrolytes, which decreases the durability. For this reason, the lifetime of molten carbonate fuel cells is short (Sundén 2019).

Direct methanol fuel cells (DMFCs) are usually powered by pure methanol mixed with water and fed directly to the fuel cell anode (Giorgi and Leccese 2013) . Unlike other cell types, most fuel storage problems are not observed in this cell type. However, working at low temperatures negatively affects efficiency. (Mench 2006),(Sundén 2019).

Solid oxide fuel cells (SOFCs) use a hard, non-porous ceramic compound as the electrolyte. This cell type operates at very high temperatures up to 1000°C . Since they operate at high temperatures, they do not need a precious metal catalyst (Sındırac et al. 2019). This reduces the cost of the system. Other advantages of SOFCs are high efficiency, fuel flexibility, mobile and fixed energy generation, carbon dioxide recycling, chemical synthesis, modularity, negligible pollution and reliability (Sundén 2019). Working at high temperatures has disadvantages. The foremost one; it's the resistance to

work at high temperatures. The development of low-cost materials with high durability at cell operating temperatures is one of the essential technical challenges facing this technology. To solve this problem, scientists are working on SOFCs with high durability that will operate at 700°C or lower temperatures (Mench 2006). Figure 1.3. shows the classifications of fuel cells.

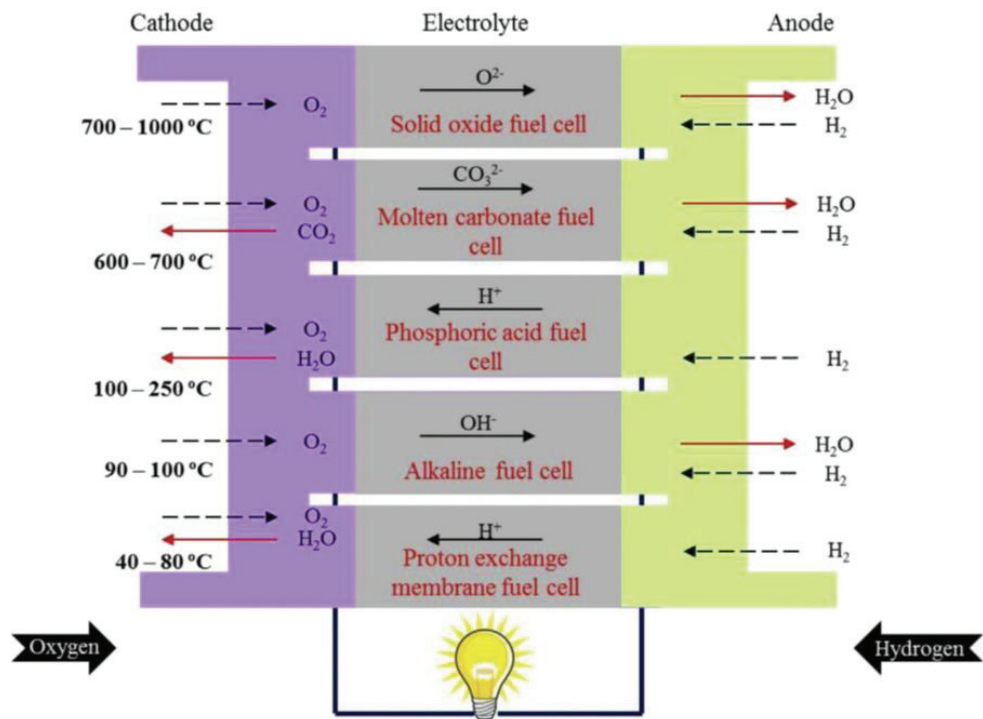


Figure 1.3. Classification types of fuel cells.

(Source: Baharuddin, Muchtar, and Somalu 2017).

1.3. Working Principle of Fuel Cells

Typical SOFC cell components; it is an electrolyte made of solid oxide ceramic material, two porous electrodes, anode and cathode, and two interconnecting wires (Figure 1.4.). Although the operating principle and components of a SOFC have similar properties to those of batteries, they differ in some respects (Giorgi and Leccese 2013). Batteries are devices that store energy. The battery's energy (electricity) production

depends on the chemical reagents in it. When these reagents are exhausted, in short, when the battery runs out, energy production stops. It needs to be charged to produce electricity again (Hoogers 2002). This is not the case for SOFCs. A SOFC will continue to generate energy as long as it is fed with fuel (hydrogen, natural gas, biogas or methane) and oxygen (or air). So charging is out of the question (Sharifzadeh et al. 2020). The electricity generation mechanism of SOFCs is based on the electrochemical combustion of the fuel (Xu 2018). The general reaction is the same as the combustion, but the reaction consists of two separate electrochemical reactions (Minh and Takahashi 1995).

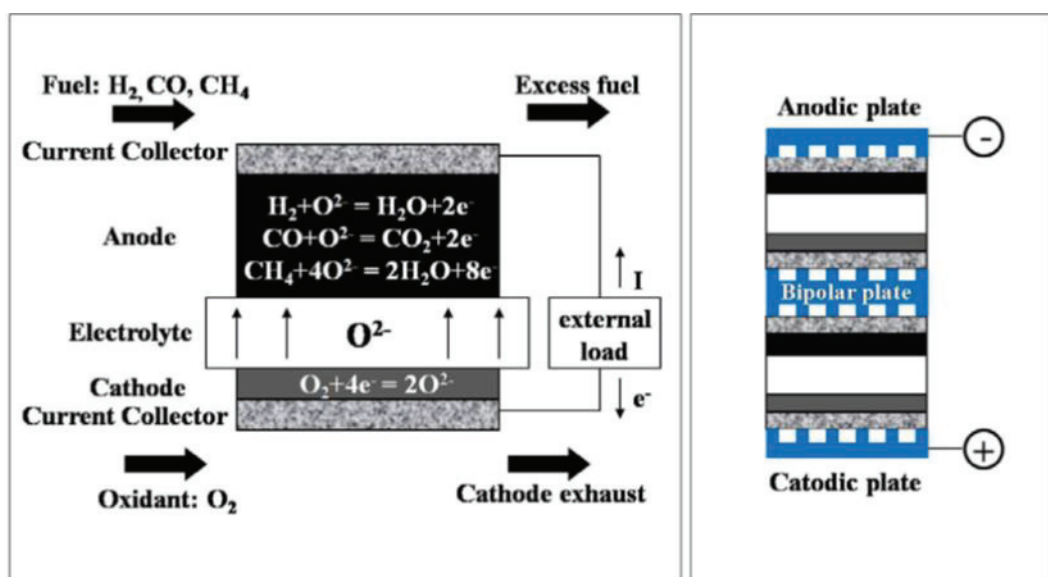


Figure 1.4. Scheme and performance of a SOFC and SOFC stack operating with different.

(Source: Tarancón 2009).

For example; the working principle of a cell using hydrogen fuel is as follows. The anode material is fed with hydrogen while the cathode material is fed with oxygen. At the anode, hydrogen dissociates into positive (H⁺) and negative (electron) ions as the oxidation of hydrogen takes place (Equation 1.) (M. Kaur, Kaur, and Kumar 2020). Positive ions migrate to the cathode by passing through the hard and non-porous ceramic electrode that does not allow electron passage. Due to the potential difference between the two electrodes, the electrons reach the cathode through an external circuit (Irshad et al. 2016). Electrons passing through the external circuit generate electricity and heat

during the transition. Electrons that tend to associate with the positive ion combine with oxygen ions (O_2^-) and reduce the oxygen (Equation 2.). The reduced oxygen ions bond with hydrogen ions and form the water molecule together. Thanks to these reactions, the system produces water, heat and electricity (Equation 3.) (Sarfraz et al. 2020).

The reaction at the anode Side (Fuel Electrode);



The reaction at the cathode Side (Air Electrode);



The overall reaction (The “redox” Reaction);



The driving force of the SOFC is the electrochemical potential difference caused by the difference in partial oxygen pressures between the electrodes. This driving force is called open circuit voltage (OCV). OCV is calculated by the Nernst equation (Equation 4. and Equation 5.). OCV is the voltage value measured when the current equals zero (Can Sındırıcıç, 2019)

$$OCV = E_0 - \frac{RT}{nF} \ln(K) \quad \text{Eq. 4.}$$

Where;

$$K = \frac{\rho_{H_2O}}{\rho_{O_2^{0,5}} \rho_{H_2}} \quad \text{Eq. 5.}$$

where R is the universal gas constant ($8.314 \text{ J.K}^{-1}.\text{mol}^{-1}$), n is the number of electrons, T represents the operating temperature in Kelvin, E_0 is the cell voltage at standard conditions, F is the Faraday constant ($9.65 \times 10^4 \text{ C.mol}^{-1}$) (Tarancón 2009), (Can Sındırıcıç, 2019). The OCV range of a SOFC cell is about 0.9-1.1 eV. Causes such as ohmic losses and polarization resistances cause polarization losses. (Tarancón 2009). Because of these losses, the practical OCV is lower than its ideal potential. Drops in OCV are indicative of deterioration in SOFC power output. If the OCV of the cell is less than 0.7 eV, there is a gas leak in the cell (Weber and Ivers-Tiffée 2004).

1.4. Why is Hydrogen Preferred?

Hydrogen is one of the most preferred fuels in fuel cells. The main reasons for this are; the fact that hydrogen is the most abundant element in nature, unlike fossil fuels, there is no danger of extinction. Hydrogen can be produced from natural and local sources. It can be used in hydrocarbons containing hydrogen instead of hydrogen for fuel in fuel cells. However, it is not preferred because it both reduces system efficiency and causes harmful gas emissions to the environment (<https://muhendistan.com/hidrojen-enerjisi-nedir/>).

1.5. Components of SOFC

SOFCS are devices with a simple design. Basically, they consist of three main components (Figure 1.5.) (Milewski and Lewandowski 2010). These are anode, cathode and electrolyte. There are primary extensive criteria that these main component materials must have. Each component must serve a variety of functions in the fuel cell and meet certain requirements. The components must have proper stability (chemical, dimensional, phase and morphological) in oxidizing/reducing conditions, as well as having chemical compatibility and suitable conductivity with each other. On the side, one of the other important features desired in these cells, which have components made of ceramic materials, is that they have similar thermal expansion coefficients in order to prevent

cracking during manufacturing and operation. The material used for the oxidation and reduction reactions that will occur in the anode and cathode regions; must be porous enough to allow the required gas passage. The desired feature of the electrolyte between two electrodes, such as a sandwich, is to have the required density to prevent gas leakage (Sındıracı, Büyükkaksoy, and Akkurt 2019). If the electrolyte is not in sufficient concentration, leaks that occur during the reactions occurring in the cell may cause a short circuit or fire. In addition to these, other characteristics required from cell components are high strength and toughness, easy fabrication and low cost (Minh and Takahashi 1995).

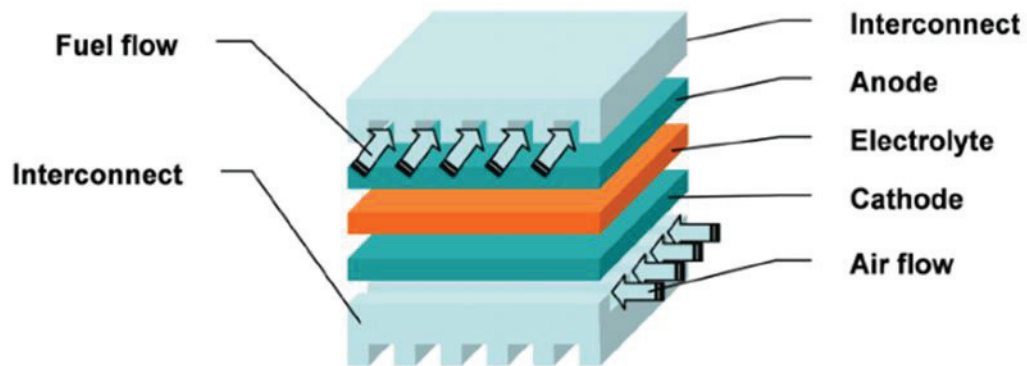


Figure 1. 5. Components that constitute a singular solid cell.

(Source: Milewski and Lewandowski 2010).

1.5.1. Anode

Fuel oxidation takes place in the anode chamber. During the selection of anode material, it is expected that the material will be able to work in harmony with SOFC cell components under optimum conditions. The reaction taking place in the anode compartment affects the cell operating performance depending on the electrochemical production of the cell. Basic properties sought in an anodic material; it should have properties such as high electronic and ionic conductivity, thermal expansion compatible with other cell components, catalytic activity, stability at high temperatures. In addition to these properties, one of the most important properties should be the optimum porosity

required for the transport (leakage) of the fuel (Dwivedi 2020). Moreover the anode is expected to show good carburization and sulfidation resistance. Important issues in anode material for various commercial applications; fuel flexibility, easy manufacturing and low cost (Zhu and Deevi 2003). Some anode materials used in fuel cells are Ni, Co, Cu and Zn based oxides (Nicollet et al. 2017). The use of the Ni catalyst as anode material in SOFCs may cause thermal expansion problem in the underlying electrolyte layer. Various methods have been developed to prevent this problem as a result of different studies. One of these methods is to prepare a mixture using Ni as anode material and YSZ, GDC, SDC , etc. materials as electrolyte material (Jamil et al. 2016). It has been observed that the prepared new cermet structure gives better results in terms of thermal expansion and electrical conductivity (Huang and Goodenough 2009b). Ni/YSZ cermet is generally used as anodic material Ni/YSZ cermet is commonly used as anodic material. Ni/YSZ cermet shows better thermal compatibility and ionic conductivity compared to other materials. Another prominent anode material in recent years has been Ni/GDC cerment. This is because the ability to suppress carbon accumulation is higher in Ni/GDC cermet than Ni/YSZ (Irshad et al. 2016), (Weber and Ivers-Tiffée 2004). Anode oxidation is shown in Fig.1.6.(Abdalla et al. 2018).

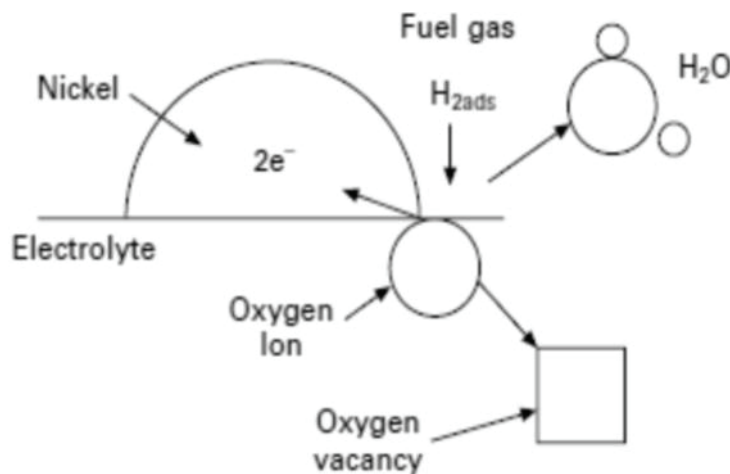


Figure 1. 6. An anode reaction scheme using H_2 as fuel.

(Source: Abdalla et al. 2018).

1.5.2. Cathode

Cathode side; It is the region where air (oxygen) enters the cell and decomposes into ions (O_2^-). The decomposition of oxygen gas into ions is known as the oxygen reduction reaction (ORR). This process as shown in Figure 1.7. it occurs in a specific region where oxygen ions, electrons and gas molecules react with each other. This zone is called the three-phase boundary (TPB) zone. The reduction reaction (ORR) of oxygen occurs as follows. First, O_2 converts to O_2^- , then the dissociated ions are moved from the cathode to the electrolyte, and finally the ions pass over the electrolyte lattice (P. Kaur and Singh 2020b). The length of the TPB process greatly affects cell performance. As the length of the TPB process increases, the reaction rate increases, which improves cell performance. Any degradation that may occur in one of the TPB phases directly affects the reaction. In such a breakdown, no reaction occurs in the cell (P. Kaur and Singh 2020a),(Dwivedi 2019).

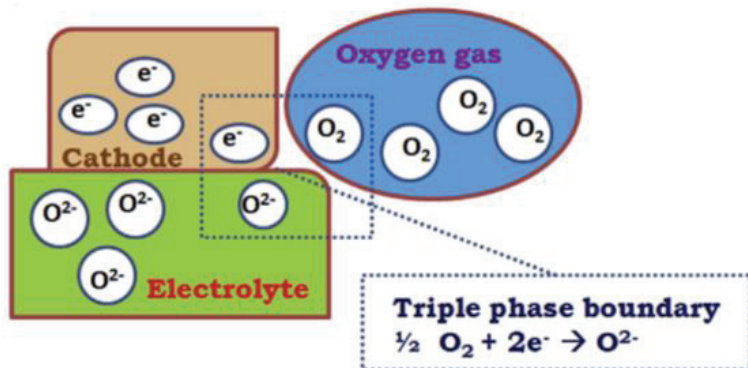


Figure 1. 7. Schematic diagram of a cathode-electrolyte interface showing the formation of a triple phase boundary (TPB).

(Source: P. Kaur and Singh 2020b).

As with the anode, the choice of material plays a vital role in the cathode. A good cathodic material is expected to have an electronic conductivity of $> 100 \text{ Scm}^{-1}$ and an ionic conductivity of $10^{-1}-10^{-4} \text{ Scm}^{-1}$. Furthermore, the thermal expansion coefficient is expected to be suitable for other cell components. Otherwise, deformations may occur at high temperatures. It is desirable that the porous electrode density be approximately 30% and 40%. The porous structure is an important element in the cells operating performance.

Because the cell is mechanical and electrical properties change according to the porous electrode structure (P. Kaur and Singh 2020a). In addition to these, in terms of being easy to apply and economic attractiveness; electrode polarization resistance should be less than $0.15 \Omega \cdot \text{cm}^2$. This situation causes great difficulties in operating the system in medium temperature conditions (Shao and Tadé 2016a).

One of the materials commonly used in SOFCs is Lanthanum strontium manganite ($\text{La}_{1-x}\text{Sr}_x\text{MnO}_3$) perovskite materials. This is because $\text{La}_{1-x}\text{Sr}_x\text{MnO}_3$ has stable structure and good running performance (Shao and Tadé 2016a). In addition, it has good chemical compatibility with zirconia-based electrolytes at high SOFC operating temperatures. Leng et al. Sintered LSCF ($\text{La}_{1-x}\text{Sr}_x\text{Co}_{1-y}\text{Fe}_y\text{O}_3$) - GDC composite cathode material at 975°C for 2 hours for SOFCs with GDC electrolyte. A pure LSCF cathode had a polarization resistance of $1.20 \Omega \cdot \text{cm}^2$ at 600°C , while an LSCF - GDC showed a much lower polarization resistance of $0.17 \Omega \cdot \text{cm}^2$ under the same conditions(Leng, Chan, and Liu 2008). This situation made the LSCF - GDC more in demand. Other commonly used cathodic materials LaNiO_3 -Based Cathodes, SrCoO_3 -Based Cathodes, BaCoO_3 -Based Cathodes (Dwivedi 2019) , (Minh and Takahashi 1995).

1.5.3. Electrolyte

The main task of SOFC electrolytes is to transmit ions by acting as a bridge between electrodes (anode and cathode). Electrolyte; it carries ions generated from one electrode to the other electrode to balance the charge from the electron flow and complete the electrical circuit in the fuel cell (Kilner, Druce, and Ishihara 2016). In addition to them, it also allows the fuel to be separated from the oxidizer in the fuel cell. Therefore a good electrolyte is desired to be stable and gas-tight (dense) in both reducing and oxidizing environments. Furthermore, it is expected to have high ionic conductivity and low electronic conductivity at cell operating temperatures. SOFCs are cells operating at high temperatures ($600\text{-}1000^\circ\text{C}$) (Minh and Takahashi 1995). Another important electrolyte property is that it must be chemically and thermally compatible with other cell components both at room temperatures and at high temperatures where the fuel cell is manufactured (Huang and Goodenough 2009a),(Shao and Tadé 2016b).

As a result of electrolyte development studies, bismuth-based oxides with high ionic conductivity, zirconia-based oxides, cerium-based oxides and lanthanum gallate-based oxides were developed. These oxygen ion-bound electrolytes can also be classified as perovskite and fluorite-based systems (Shao and Tadé 2016b). Fluorite-based systems are usually written as AO_2 . One of the commonly used electrolyte materials is zirconium dioxide. ZrO_2 (zirconium dioxide) has three known morphological structures. It is known that zirconium dioxide, which has a monoclinic crystal structure at room temperature, changes its morphological structure with temperature. monoclinic $<1170^\circ\text{C}$, tetragonal $1170\text{--}2370^\circ\text{C}$, and cubic $>2370^\circ\text{C}$ (Minh and Takahashi 1995). Some oxides used with zirconium are; it is $\text{CaO}, \text{Sc}_2\text{O}_3, \text{Y}_2\text{O}_3$ (Shao and Tadé 2016b). Perovskite crystal structure is written as ABO_3 (M. Kaur, Kaur, and Kumar 2020), (Ishihara, Sammes, and Yamamoto 2003). Another widely used electrolyte material is $\text{LSGM-La}_{0.9}\text{Sr}_{0.1}\text{Gd}_{0.8}\text{Mg}_{0.2}\text{O}_3$ (lanthanum strontium gallium magnesium oxide) in provskite structure. LSGM conductivity is higher than doped zirconia electrolyte. The electrical conductivity of LSGM is improved by incorporating some selected additives such as Ni, Co and Fe into its matrix (M. Kaur, Kaur, and Kumar 2020). CeO_2 (Cerium oxide) has a fluorite type crystal structure. Compared to other pure oxides, ceria is stable up to its melting point of 2100°C (Mench 2006). Compared to zirconia-based electrolytes; they have good conductivity with electrodes. Additives commonly used in cerium-based compounds; $\text{CaO}, \text{MgO}, \text{BaO}, \text{SrO}$, and GdO (M. Kaur, Kaur, and Kumar 2020).

1.6. Sintering and Densification in Ceramic Materials

Ceramics are generally manufactured from oxide-based raw materials (e.g. Al_2O_3 , SiO_2 , CeO_2 , etc.). This is because there are naturally more oxides than the earth's crust because there is oxygen in the air and natural rocks are also oxide-based. Melting oxides requires higher temperatures compared to metals. For this reason, ceramics cannot be produced by traditional methods used for metals such as melting and casting while shaping. Therefore, unlike metals, ceramics are produced by fusing powder particles together. Powder particles require high temperatures and very high surface areas to fuse, but still these temperatures are lower than the melting temperature. This makes economical manufacturing possible.

Before sintering, the powder must be shaped in order to turn it into the final product. The most common forming methods are dry pressing, extrusion, strip casting, slip casting, etc. with increasing water/solid ratio. Countable. The use of water here is necessary because it allows the powder to take a three-dimensional shape. The moist powder compact that is shaped should be dried before cooking. For this, drying processes where temperature and humidity are strictly controlled are applied. The dried powder compact is called "green ware" and must be fired at high temperatures to increase its strength and density (Ref: Jones Berard Industrial Ceramics, Kingery, James Reed). The partial density of green ceramic contains 25-60% pores. These pores must be reduced in order to improve the strength, thermal conductivity, electrical properties and other properties of the material. This improvement is achieved by sintering the material at high temperatures (Kingery, Bowen, and Uhlmann 1976).

The sintering process is the process of reducing the porosity and increasing the density of powder particles that touch each other by firing at a temperature below the melting temperature of the material. This temperature corresponds to 0.5 (1/2) to 0.7 (2/3) times the melting temperature of the material in Kelvin. Sintering is a one-way process. As seen in Figure 8 , two particles in contact with each other are seen (Kang 2010). As the sintering process progresses, bonds are formed between the particles in contact with the effect of temperature. As the process continues, grain boundaries form and grow at these contact points. As a result of sintering, these two particles completely combine, resulting in the formation of a single particle with 1.26 times the initial radius (Figure 1.8.). The main driving forces in sintering are the reduction of the surface area of the powder particles and the heat approaching the melting temperature. Due to their very high surface area ($1-1000 \text{ m}^2/\text{g}$), dust particles tend to bond if little heat is supplied. It is known that some very fine-grained ceramic powders can be sintered even at temperatures such as 400°C (Nano Zirconia sintering).

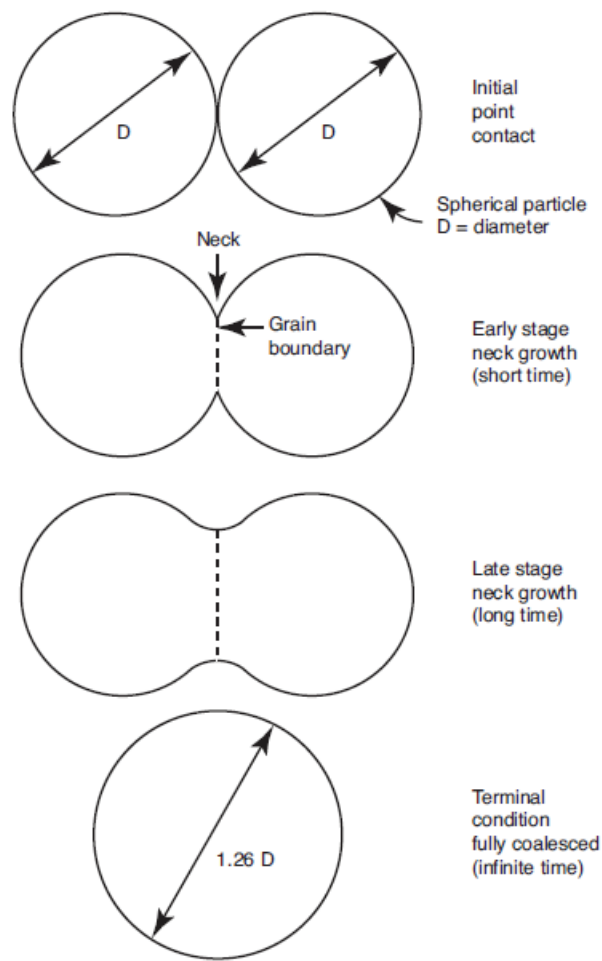


Figure 1. 8. The stages of neck formation of two powder particles by sintering and the combination of powders to become a single powder with a diameter of 1.26.

(Source: Kang 2010).

1.6.1. Sintering Process

The sintering process takes place in three stages.

Stage 1: The first stage is the smoothing of the particle surfaces and the observation of the neck formation by diffusion, vapor transport and plastic flow between the particles touching each other. At this stage the porosity decreases by 12%, the theoretical density is close to 65%. No grain growth is observed in the first stage of sintering.

Stage 2: In the second stage, the surfaces that the particles come into contact with increase thoroughly. Grain boundaries are formed to a large extent. Porosity is significantly reduced. Before the final stage, the theoretical density is approximately 90%.

Stage 3: In this stage, there are closed pores in the intergranular structure. Pores remaining in the closed area are eliminated by diffusion at the grain boundaries. In addition, as most of the initial surface energy is consumed, the sintering speed is slow and the material is 92-95% denser (Kang 2010),(M.N. Rahaman 2010).

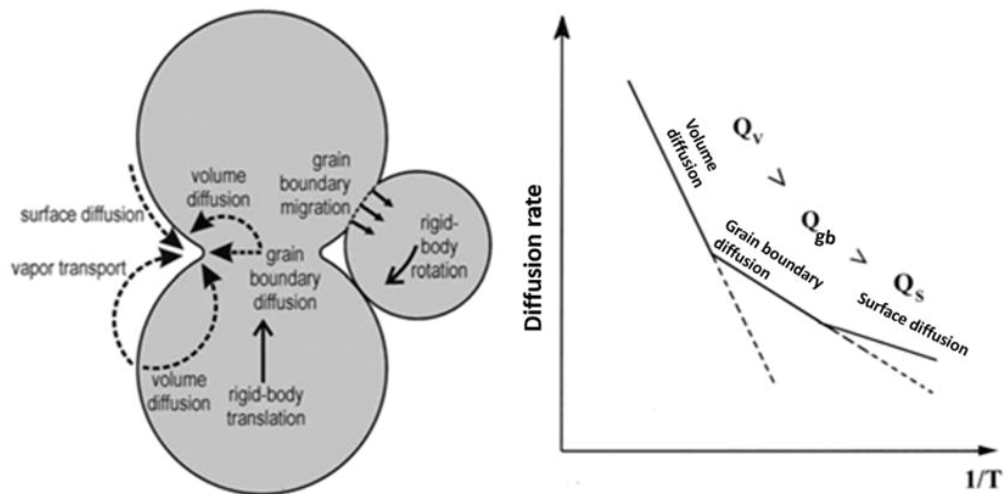


Figure 1.9. Sintering mechanisms and dependence of the dominant mechanism on the sintering temperature.

(Source: Kumar 2008).

As can be seen in Figure 1.9, diffusion occurs faster on the surface compared to the grain boundaries or the volume diffusion. Different migration pathways are also shown. It is the migration of atoms from inside the particles to the neck area that leads to volumetric shrinkage (Kumar 2008).

Unit volume surface energy in powder particles is inversely proportional to the particle diameter. Therefore, smaller particles with a high specific surface area have more energy and sinter faster (Kumar 2008).

1.6.2. Solid State Sintering

There are three types of sintering with different densification mechanisms. These are solid phase sintering, liquid phase sintering and reactive sintering. This section will focus on solid phase sintering.

Solid-phase sintering: occurs when shaped powders approach each other with the help of heat treatment, join together and close the porosity between them. The dimensions of the shaped powder particles and therefore their surface energies are different from each other. Every substance in nature wants to reach the minimum energy (steady state) level. If the material is subjected to high heat treatment, the driving force required for diffusion (diffusion) is created. In this way, a large number of small particles combine with each other to increase the grain size and decrease the surface free energies as the active surface area decreases. In solid state sintering, mass transport occurs by volume and grain boundary diffusion. Driving force is the difference between surface free energies.

Solid state sintering mechanism, the driving force required for densification depends on the reduction of the global surface energy. Driving forces for mass transport are differences in pressure and concentration gradients of point defects (pores) due to differences in the radius of curvature of microstructured particles. As seen in Figure 1.10.; neck base is concave. concave surface seeks to pull itself on a flat surface. The sphere surface away from the neck is convex with an inverse curvature. The sintering microstructure consists of a mixture of convex and concave surfaces. The natural tendency during sintering is to remove gradients. The tension in the neck area is different from the adjacent area. Therefore, the curvature gradient during sintering gives the gradient that drives the mass flow. Atomic movements happen to remove the gradient. As the temperature increases, the atoms flow from the convex surface to the concave surface. Temperature and atomic motion are directly proportional. In other words, as the temperature increases, so does atomic motion and sintering accelerates.

Unit volume surface energy in powder particles is inversely proportional to the particle diameter (Kumar 2008). Small particles are sintered faster because they have large gradients and higher energy (Sundén 2019),(Kang 2010).

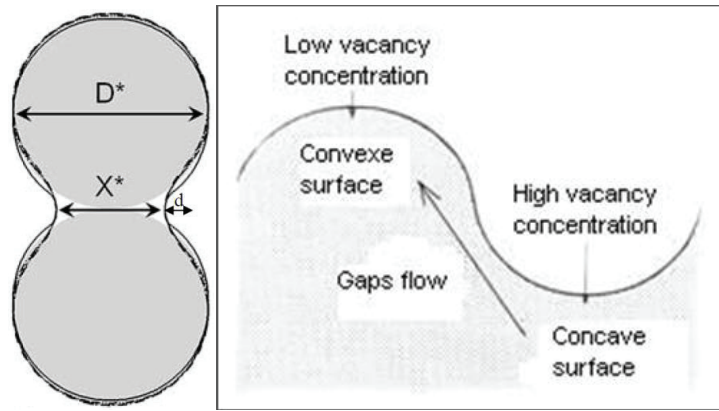


Figure 1. 10. A representation of the transport of mass from a convex to a concave surface.

(Source: Kumar 2008).

The path used for mass transport is shown in Figure 1.11. These pathways consist of surface, lattice and grain boundary diffusion as well as vapor phase diffusion. These ways lead to the formation of different sintering mechanisms. Each of these mechanisms is used to establish the kinetics of sintering (M.N. Rahaman 2010).

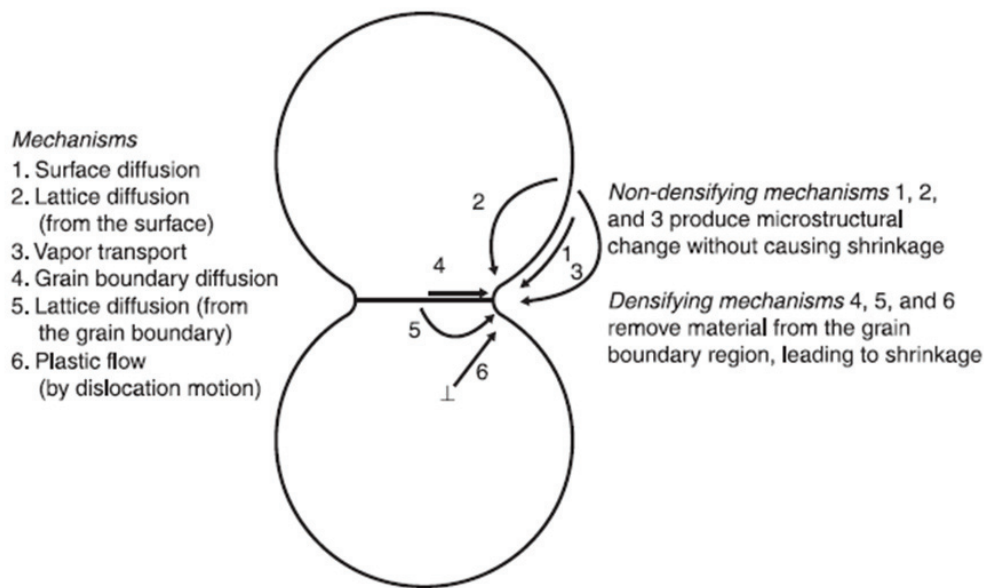


Figure 1. 11. A demonstration of the sintering mechanism.

(Source: M.N. Rahaman 2010).

Kinetic data are practical and theoretically important for densifying powder during sintering. Using dilatometric analysis, the density of the material can be analyzed with functions of time or temperature. With this method, the shrinkage in the material ($\Delta L/L_0$), the first length taken from the sample and the length i after leaving the dilatometer gives information about the density of the material (Yalamaç 2010). Equation 6. densities are calculated from shrinkage data recorded using densification velocity curves, final density measurements:

$$\rho(T) = \rho_f \left(\frac{1 + \frac{\Delta L_f}{L_0}}{1 + \frac{\Delta L_{f(T)}}{L_0}} \right)^3 \quad \text{Eq. 6.}$$

In the formula, L_0 is the first sample length, L_f is the last sample length, and $L_{(T)}$ is the sample length at temperature T .

In order to obtain the densification ratio, the relative density is derivatized according to the temperature. In Equation 7., the derivative equation of relative density according to temperature is given (Yalamaç 2010).

$$\frac{d\rho(T)}{dT} = -3 * \frac{d\left(\frac{\Delta L(T)}{L_0}\right)}{dT} * \frac{\left(1 + \frac{\Delta L_f}{L_0}\right)^3}{\left(1 + \frac{\Delta L(T)}{L_0}\right)^4} * \rho_f \quad \text{Eq. 7.}$$

Caisso et al. investigated the possible effects of different compression pressures on green pellet microstructure and sintering behavior. Low compression pressures resulted in green pellets of low mechanical cohesion as shown in Figure 1.12 below. This prevents good densification and results in low final densities (Caisso et al. 2017).

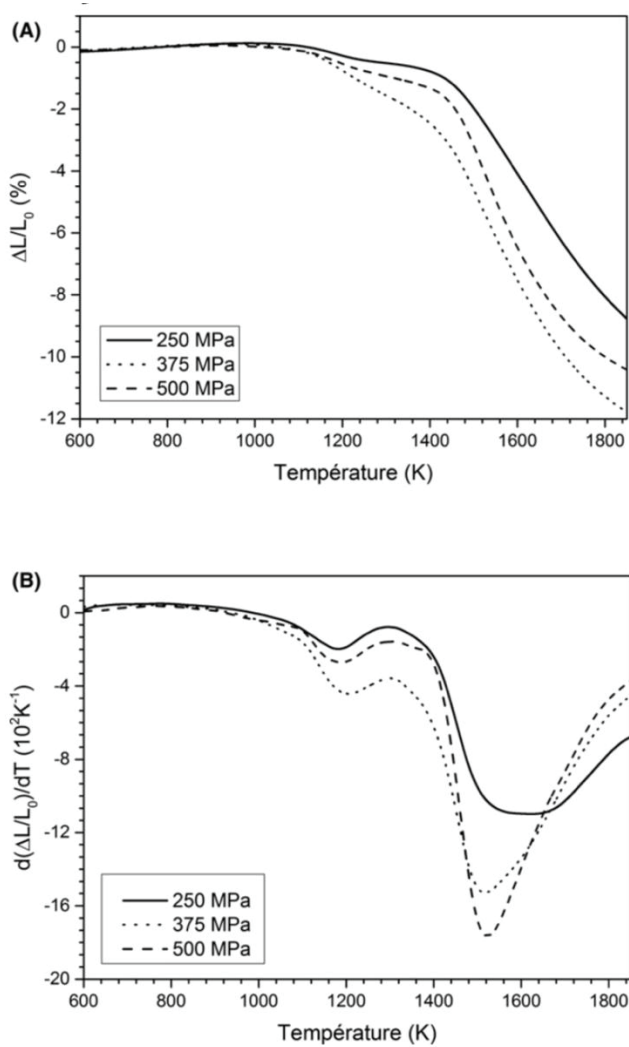


FIGURE 8 Densification curves (A) and Shrinkage rate curves (B) during sintering under air of Ce_{0.8}Gd_{0.2}O_{1.9} microspheres converted at 1073 K and pelletized at different pressures

Figure 1. 12. Densification curves (A) and Shrinkage velocity curves (B) of Ce_{0.8}Gd_{0.2}O_{1.9} are given.

(Source: Caisso et al. 2017).

1.7. Thermal Expansion Measurement with Dilatometer

Dilatometer, is a device used to measure the change in the size of the sample depending on the temperature or time. With this device, the linear thermal expansion coefficient, glass transition temperature, softening and expansion/shrinkage/penetration

behavior of materials can be determined (Figure 1.13) (<https://merlab.metu.edu.tr/tr/dilatometer>).

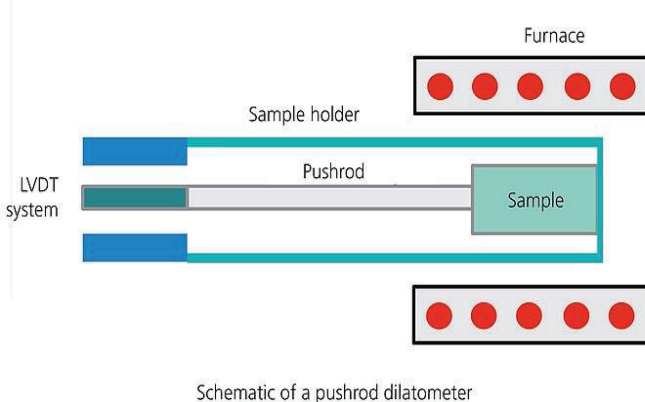


Figure 1. 13. Schematic representation of a dilatometer device.

(Source: <https://www.netzsch-thermal-academy.com/en/advanced-materials-testing/methods/dilatometry/>)

They are widely used in many areas such as glass and ceramic industry, sintering of high-tech ceramics, aviation industry, research of new materials. Due to its reliable results, it has been widely used in the investigation of the behavior of ceramic materials. Sudden temperature changes are not desired in ceramic materials. One of the reasons for this is the occurrence of cracks in ceramics. It is possible to observe the expansion/contraction behavior of ceramic materials during sintering in a correct and healthy way with this device.

1.7.1. Working Principle of the Dilatometer

For dilatometric analysis, the sample is placed in a special holder in a mobile furnace. A push rod is positioned directly against the sample and transmits the length change to the linear variable displacement transducer (LVDT). As the sample length changes during the temperature program, an output signal proportional to the displacement in the LVDT is recorded (Yalamaç 2010). The temperature program is

controlled using a thermocouple located next to the heating element of the furnace or next to the sample. Since the front of the specimen holder and pushrod are subjected to the same temperature program as the specimen, they also expand at the same time. The resulting dilatometer signal is the sum of the length changes of the sample, sample holder and push rod. To calculate the change in length in the sample; it is found by subtracting the longitudinal expansion data at the temperature at which the dilatometer is operated without a sample, without the total length expansion (Hunkel, Surm, and Steinbacher 2018), (Van der Zwaag, S., 2012), (Yalamaç 2010).

Longitudinal expansion:

$$\Delta L_{\text{corrected}} = \Delta L_{\text{sample}} - \Delta L_{\text{blank}} \quad \text{Eq. 8.}$$

here, the longitudinal expansion occurring in the $L_{\text{corrected}}$ material, the total lengthwise expansion occurring in the ΔL_{sample} material, is the amount of change in length that occurs when the ΔL_{blank} dilatometer is operated at the desired test temperature.

Expansion coefficient:

$$\alpha = \frac{\Delta L}{\Delta T} \times \frac{1}{L_0} \quad \text{Eq. 9.}$$

Where ΔL is the change in length of the sample, L_0 is the orginal sample length and ΔT is the temperature interval.

1.8. Infiltration Process

Densification of ceramics during sintering occurs at a rate commensurate with the surface area and fineness of the powder particles. Rate of densification usually increases at temperatures higher than half of the melting point (Mohamed N. Rahaman 1989).

Achieving higher densities at lower temperatures has many advantages like savings in kiln energy. Therefore, different studies have been conducted to boost sintering rate at lower temperatures by using very fine starting powder, two step sintering and so on (M.N. Rahaman 2010),(Chen, Nasrallah, and Anderson 1994). The latter involves sintering the starting powder compact to an intermediate temperature to secure about 50-60% theoretical density. This semi-fired pellet is also known as a porous scaffold which is to be loaded by nano particles to further increase densification rate (Chen, Nasrallah, and Anderson 1994). This approach was first proposed by Anderson and co workers who wanted to reduce the densification temperature of fuel cell ceramics by producing a porous scaffold that is in turn loaded (infiltrated) several times with a polymeric infiltration solution followed by heating at about 400°C to drive off volatiles and precipitate the salts within the pores(Chen, Nasrallah, and Anderson 1994). In other words, porous ceramics are infiltrated with a solution to precipitate nano-sized powders to improve densification rates. The reason for using a polymeric solution is its ability to penetrate further into the pores due to its better wetting ability (Chen, Nasrallah, and Anderson 1994). After heating, salts precipitate in the pores in nano sizes which are prone to rapid dissociation and conversion into nano sized oxide particles during the second heating stage. So the two stages are as follows: (1) Loading of the pores with nano particles, and (2) Second stage heating to continue sintering of the porous scaffold. Eventually the two-step sintering process splits the sintering process into two stages. When nano-sized ceramics are present in the pores, they activate earlier during the sintering process than the main ceramic compact. Earlier activation allows the density to increase even before reaching the final temperature. The polymeric GDC solution used for the infiltration process in this study contains Ce^{4+} and Gd^{3+} salts. This solution infiltrates the porous scaffold as seen in Figure 1.14.a. After the infiltration process, the porous scaffold is heated at 400°C. The purpose of this process is to evaporate the solvents in the solution. After the heating process, a new GDC film layer is formed inside the pores (Figure 1.14.b.). Infiltrated porous scaffolds are finally sintered at 1400°C in order for solid state diffusion to take place and reach the final density. It is thought that the applied infiltration increases the sintering rate for three reasons. 1) Salts leaking into the porous scaffold fill the pores, causing a denser structure to form. 2) As they fill the interparticle space, they act as a bridge between the particles and facilitate neck formation. 3) The resulting film layer provides a rapid diffusion path for the amorphous structure of the

GDC particles (Sındırıcı et al. 2019). The advantage of the infiltration process is that it contains the same cations as the host infiltrating the scaffold. In other words, it does not contain any additives that may affect the electrical and thermodynamic properties (Chen, Nasrallah, and Anderson 1994),(Buyukaksoy and Birss 2016).

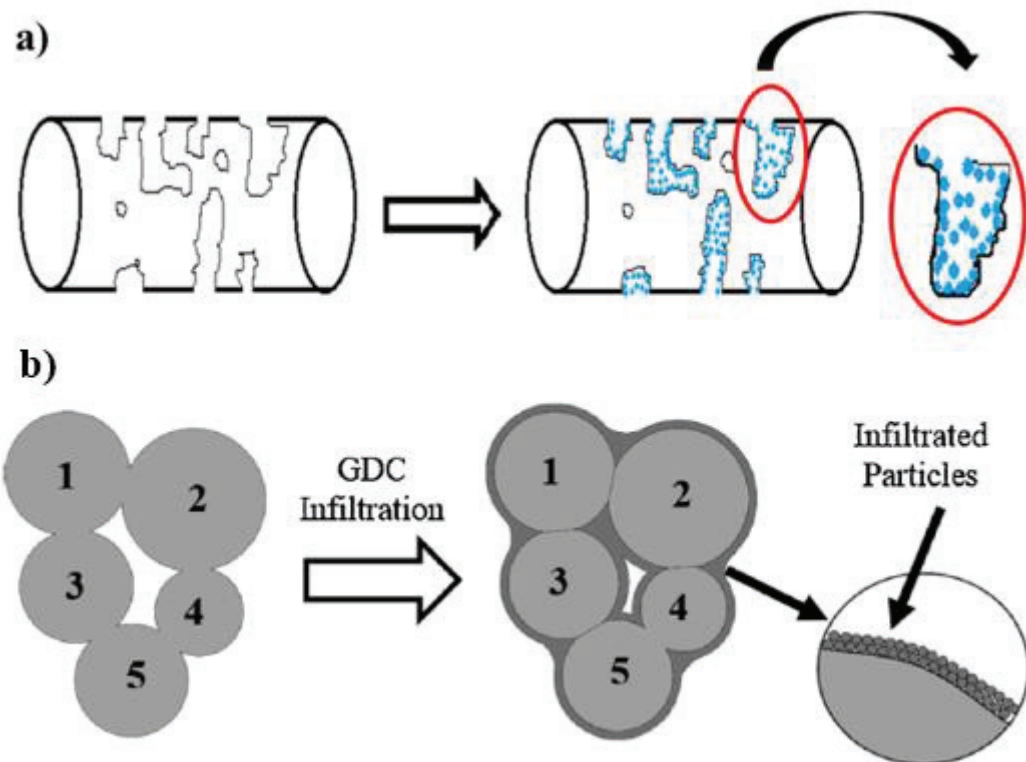


Figure 1. 14. a) Leakage of solution into the porous structure. b) Formation of an interparticle film layer after infiltration.

(Source: Sındırıcı et al. 2019).

In this thesis, GDC ceramics that are normally densified above 1450°C in ambient atmosphere are hypothesized to be densified earlier at a lower temperature via the help of infiltration of semi-fired GDC scaffolds.

CHAPTER 2

EXPERIMENTAL METHODS

GDC was obtained in powder form from the supplier (Fuelcellmaterials.com). Characteristics of this powder are explained in section 2.2.1. This powder (Code: GDC10-TC) was analyzed for its chemistry and structure before being compressed into a cylindrical shape for dilatometric analysis. Results are shown in the next section. Compressed pellets were then treated by two different methods: (1) They were directly placed inside a vertical dilatometer for densification measurements, and (2) they were sintered at a low temperature just enough to impart sufficient strength to the pellet before infiltration with a GDC bearing solution. The purpose of infiltration is explained in detail in the literature review section Chapter 1. Figure 2.1 shows the experimental steps followed throughout the thesis.

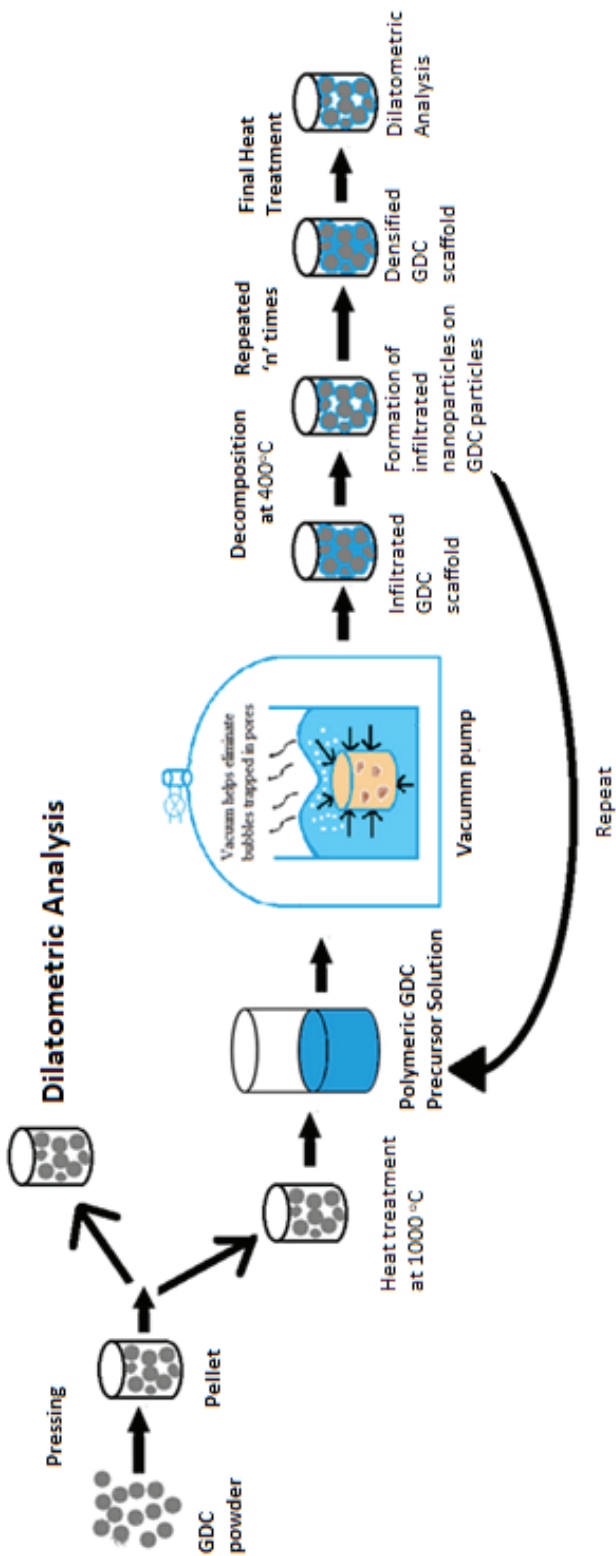


Figure 2. 1. Schematic representation of the experimental steps followed in this thesis.

2.1. Fabrication of Porous GDC Scaffold Electrolyte

2.1.1. Preparation of Pellets

10 mol % gadolinium doped ceria – tape cast grade powder ($\text{Gd}_{0.10}\text{Ce}_{0.90}\text{O}_{1.95}$) was used for preparing the porous ceramic scaffolds. Theoretical density of 10 mol% gadolinium doped ceria is taken as 7.2 g/cm^3 (Prasad et al. 2010a). Specific surface area of this powder was $6.1 \text{ m}^2/\text{g}$ while the d_{10} , d_{50} and d_{90} values were $0.11 \mu\text{m}$, $0.20 \mu\text{m}$ and $0.38 \mu\text{m}$ respectively. To shape the green powder into pellets, it was pressed in a cylindrical stainless steel die of 5mm diameter and about 7.5mm height by uniaxial pressing (Carver Hydraulic Press, Wabash, IN, USA) with a pressure of 340 MPa (1500 pounds) (Figure 2.2.).

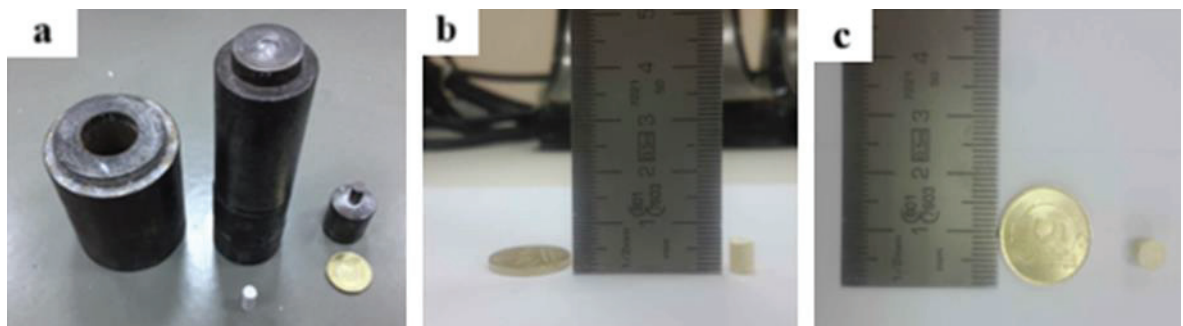


Figure 2. 2. a) Steel mold used to prepare 5mm long pellets. b) and c) view from different angles of the dimensions of pelletized GDC powders.

After this step, two different groups were formed as seen in Figure 2.1. One of these groups was the non-infiltrated group (A group) and the other was the infiltrated group (B group). These groups are classified in more detail in Tables 2.1 and 2.2.

Table 2. 1. Group A non-infiltrated GDC sample codes.

A Group Code Number	Final sintering temperature with dilatometer (°C)
GDC-A1	1250
GDC-A2	1400

2.1.2. Polymeric Precursor Solution Preparation

The polymeric GDC precursor solution infiltration method was used to densify the porous GDC scaffolds. To prepare the polymeric GDC precursor; The Ce(NO₃)_{3.6}H₂O (ALDRICH 99%) and Gd (NO₃)_{3.6}H₂O (ALDRICH 99%) salts were dissolved in deionized water at a certain molar ratio of cations. Then Gd_{0.10}Ce_{0.90}O_{1.95} (GDC) to obtain stoichiometry; the salt solution was mixed with ethylene glycol at molar ratios = 0.020-0.080: 1 (Sındırıcı et al. 2019). The resulting mixture was mixed at 80°C until all the water in it evaporated and polymerization took place. The mixture was weighed at certain intervals to understand how much of the water in it evaporated (Buyukaksoy and Birss 2016). Determination of mixing ratios is purely experimental. Than the solution was diluted with 2-butoxyethanol (1:1 weight ratio) (in order to ensure good wetting properties of GDC scaffold and for reducing the surface tension of the polymeric solutions (Chen, Nasrallah, and Anderson 1994).

2.1.3. Dilatometric Analysis of non-Infiltrated GDC Pellets (Group A samples)

Pellet sample GDC-A1 was sintered in a Linseis L75 vertical dilatometer up to 1250°C by heating and cooling at a rate of 3°C/min (Linseis Co., Germany). The second sample (hereinafter called GDC-A2) was sintered up to 1400°C using the same heating and cooling rates. Sample codes are as shown in Table 2.1.

2.1.4. Creation of Porous Scaffolds from Infiltrated GDC Pellets (Group B Samples)

Group B pellets were sintered in an electrically heated laboratory furnace (Nabertherm LHT 02/17, Germany) to form porous scaffolds (Figure 2.3.a). The heating and cooling rates were 2.71°C/min while the dwell temperature was 1000°C and dwell time was 8 hours. Figure 2.3.b. shows the newly formed porous scaffold specimen. Further experiments were conducted using this porous scaffold. These are GDC-B3 and GDC-B4. After this step, both groups were infiltrated with 0.02 M Polymeric precursor solution with different number of infiltration cycles. The infiltration process will be discussed in detail below. Sample codes are given in Table 2.2.

Table 2. 2. Group B infiltrated sample codes.

B Group	Code Number	Infiltration			Temperature	
		Number of cycles	Solution Types	Solution concentration (M)	Initial heat treatment (°C)	Final heat treatment (°C)
Infiltrated samples	GDC-B3	40	GDC	0.02 M	1000	1400
	GDC-B4	50	GDC	0.02 M	1000	1400

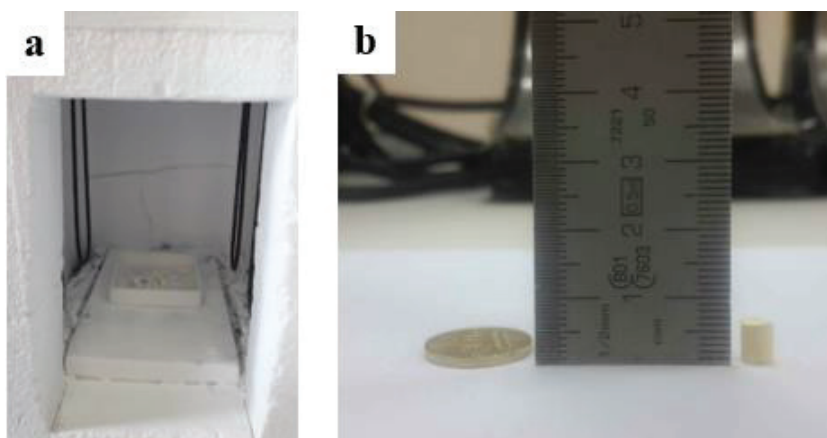


Figure 2. 3. a) Box furnace used for sintering GDC pellets which were sintered at 1000°C to form the porous scaffold. b) The GDC porous scaffold.

2.1.5. Infiltration Process

Figure 2.4. shows schematically the infiltration process of porous GDC by GDC precursor solutions, respectively. This process was applied to group B pellets. The semi-sintered GDC scaffold was immersed in GDC precursor solutions. It was then placed in a vacuum pump (Lanphan 2XZ-2, Zhengzhou, Henan, China) to facilitate the evacuation of air bubbles trapped in open pores. Thus, the precursor solution replaced the air bubbles. Figure 2.5.b. shows images from different steps of this process that took approximately 10 minutes to complete.

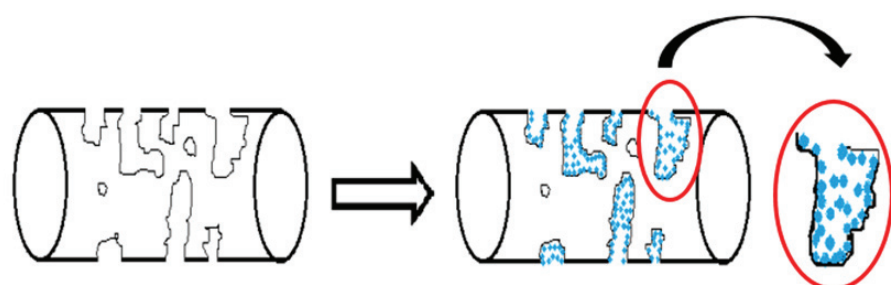


Figure 2.4. Simple demonstration of infiltration of air pockets within a semi-fired scaffold.

After the vacuuming process was over, excess solution on the wet scaffold was removed from the polymeric precursor solution with a damp napkin. A dry napkin would have sucked all moisture from the pores. The moist scaffold was then placed on a heater. The heater was maintained at 400°C with a dwell time of 10 minutes. Heating and cooling rates were 5°C/min. The heater was used to evaporate all the solvent in the scaffold. This procedure was repeated several times (40x and 50x depending on the sample code) before the samples were placed in the dilatometer. All dilatometer experiments were done with 3°C/min of heating and cooling rates. Final soak temperatures varied depending on the sample. After the infiltration process was completed, the samples were subjected to a final heat treatment at 1400°C (without dwelling at the maximum temperature) using a vertical dilatometer. The pellet infiltrated 40 times was hereafter called GDC-B3 while the pellet infiltrated 50 times was called GDC-B4. The experimental steps are shown step by step below (Figure 2.5.).

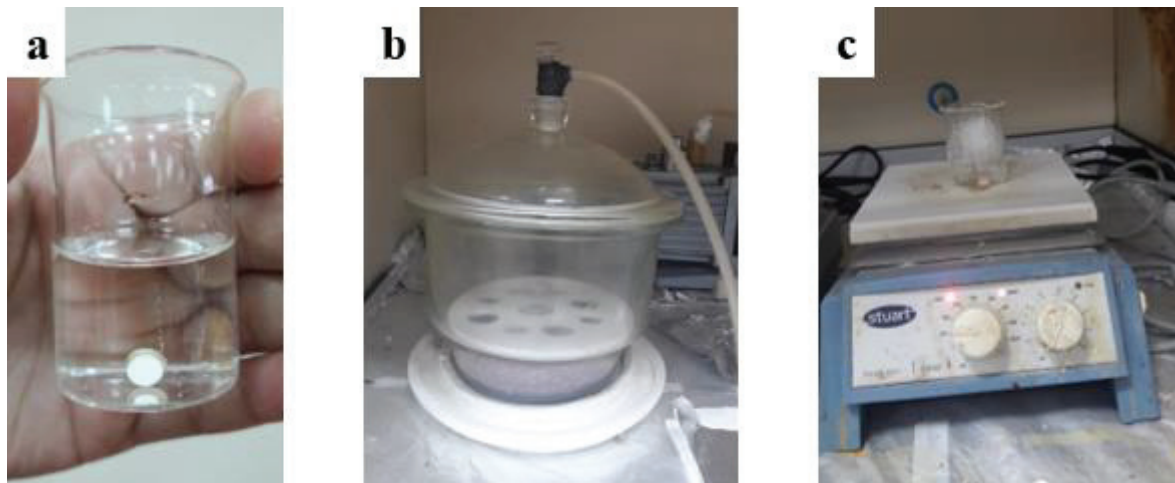


Figure 2.5. a) Immersion of the porous GDC scaffold into the precursor liquid. b) Filling the inside of the pores with liquid by vacuuming. c) Removing the solution and other organics from the pellets.

2.1.6. Weight and Density Measurements

The final density of pellets were measured by the Archimedes method according to ASTM C-20 standard (Figure 2.6.) (ASTM International 2000).

First, the weight, length and diameter of the pellet (sample) to be tested were measured before processing.

The pellet was dried in an oven at 110°C for 24 hours to measure the dry weight (D). Then it was weighed again and its dry weight was noted.

Suspended Weight (S), the sample was placed in a container with 40 ml of pure water and heated to 100°C at a heating rate of 4°C/min. After boiling at 100°C for 5 hours, it was cooled down at the same heating rate. It was then weighed again and the data was noted.

To measure Saturated Weight (W), the sample taken from pure water was removed with the help of a moist paper towel. The moist sample was weighed and its data noted.

$$V=W-S$$
 Eq. 10.

found with exterior volume value with Equation 10.

Based on these data bulk density was calculated (Equation 11.).

$$B=D/V$$
 Eq. 11.

After the density measurement of samples, relative density was estimated by using the Equation 12.

$$\% \text{Relative Density} (\% RD) = (d_s/d_{th}) * 100$$
 Eq. 12.

where d_s is the measured bulk density of sample and d_{th} is the theoretical density of GDC. Theoretical density of 10 mol % gadolinium doped ceria is taken as 7.2 g/cm^3 (Prasad et al. 2010a).

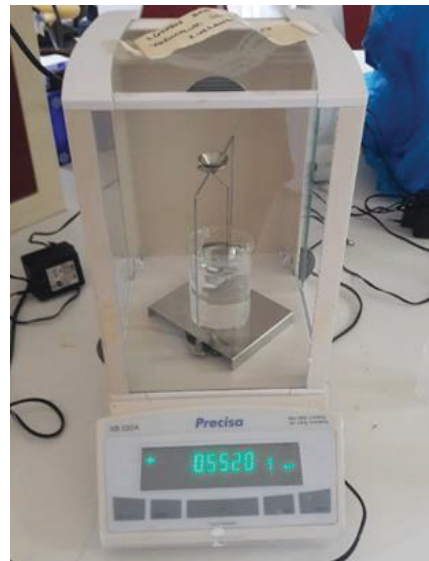


Figure 2. 6. Measuring weight with Archimedes method.

2.1.7. Structural and Microstructural Characterization

The crystal structure of GDC powder was examined by X-Ray Diffraction (XRD, Panalytical X-Pert Pro). Cu K α radiation was used as the X-Ray source. Secondary electron (SE) imaging and Energy Dispersive X-Ray Spectroscopy (EDX) were used for the composition analysis of the powder. Scanning Electron Microscopy (SEM, Philips XL 30S FEG) was used for microstructural analysis of infiltrated and non-infiltrated GDC samples.

CHAPTER 3

RESULTS AND DISCUSSION

Results of all experimental work is presented in this chapter in the order of processing of the samples. First the properties of the as-received powder and its compaction into a pellet form is explained. Second, results obtained from sintering of this pellet into a porous scaffold structure and its infiltration with the polymeric precursor solution are given. As described in Chapter 2, there were two main routes for the experiments: (1) direct sintering of the compressed pellet and (2) sintering of the infiltrated porous pellet. Experimental results and their differences from each other are discussed.

3.1. SEM Analyses

Pressed pellets were sintered in a box furnace in ambient atmosphere at 1000°C for 8 hours. The porous samples came out of the furnace with marginal strength and integrity because they were sintered at the lowest possible temperature to produce a porous scaffold. Therefore their densities could not be measured by Archimedes method which required boiling for extended periods in water. These porous scaffold samples were weighed and their dimensions were measured to calculate their densities which showed that they were 60% of their theoretical densities with 4.3 g/cm³. Figure 3.1. shows SEM image of green as-received GDC powder. Figures 3.2.a and 3.2.b the structure of the porous scaffold fired at 1000°C and SEM analysis of this sample.

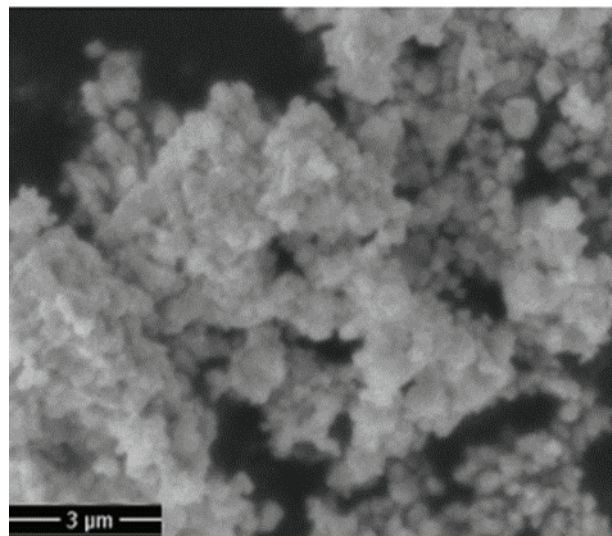


Figure 3. 1. SEM image of the untreated as-received green GDC powder. Agglomerate formations are observed in the sample.

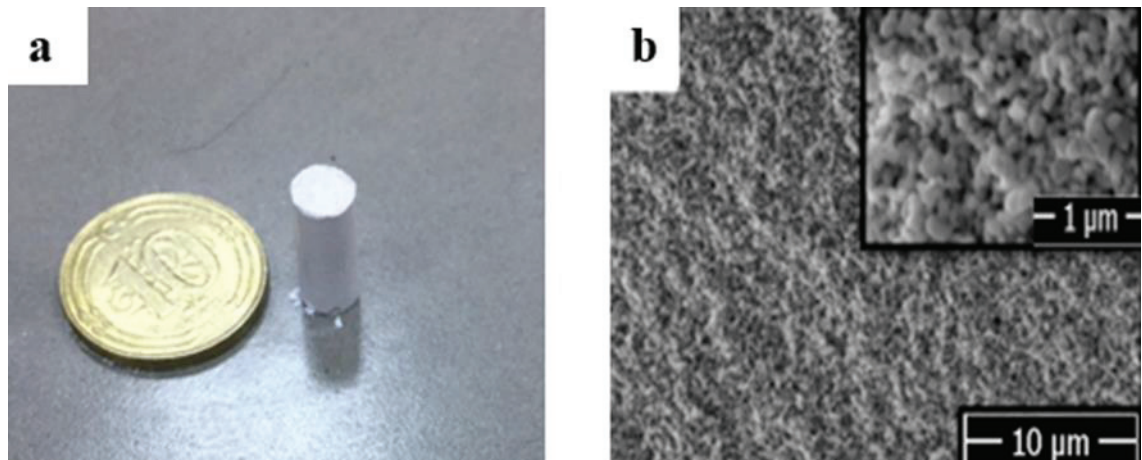


Figure 3. 2. a) Porous GDC pellet sintered at 1000°C and b) SEM image of this pellet.
(Source for Figure 3.2.b: Sındırac et al. 2019).

Porous GDC scaffolds were studied in two different experimental groups. The first group (group A) was heat treated and sintered at different temperature values. The sintering behaviors of these groups at different temperature values were investigated. GDC polymeric precursor solution was used again to infiltrate the second group (group B) porous GDC scaffold. A different number of infiltration cycles were carried out in the second group. Later, this group was subjected to sintering process.

GDC pellets used in both groups were pressed at 340 MPa pressure. Although these two groups are operated at different temperatures in the dilatometer, the heating and cooling rates were both 3°C/min. Figure 3.3. shows the SEM images of all samples' fracture surfaces.

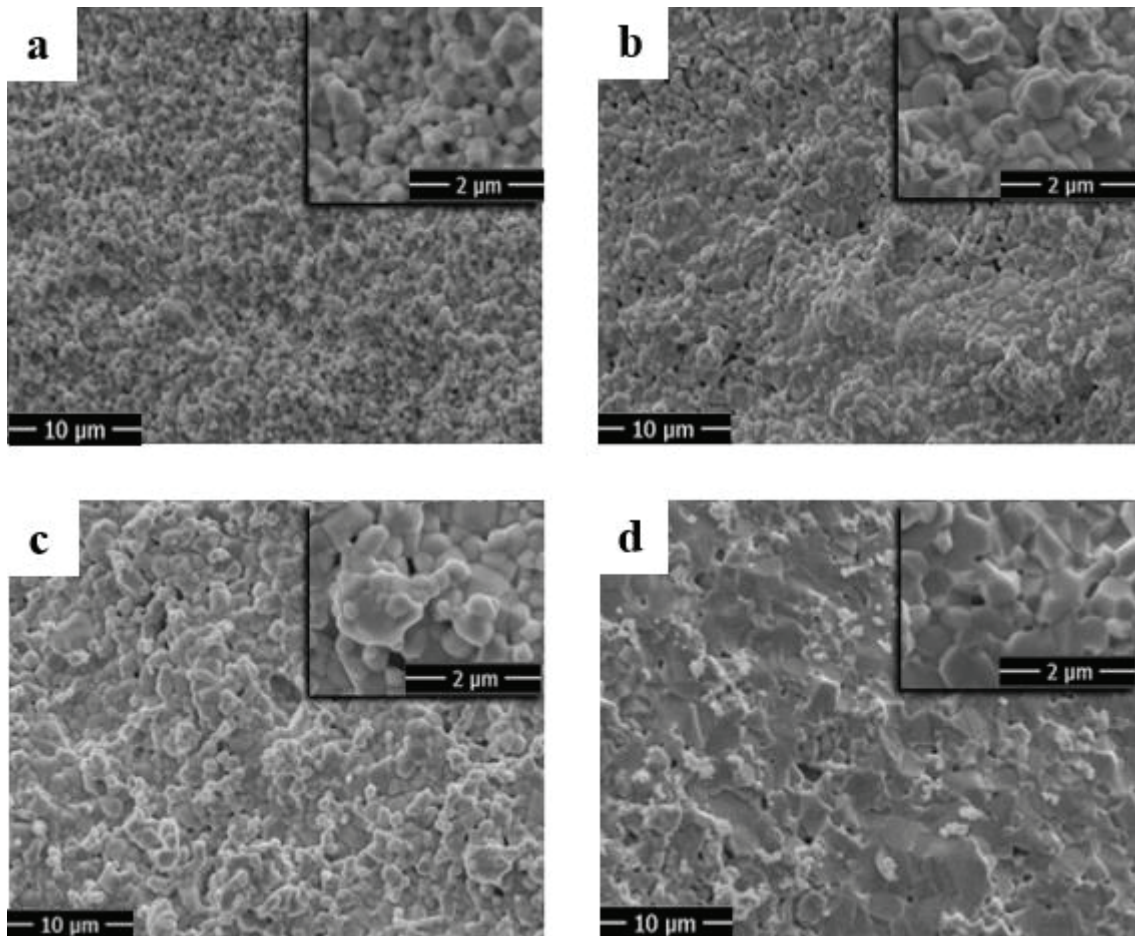


Figure 3.3. SEM images of fracture surfaces of sintered samples. a) GDC-A1 sample after 1250°C heat treatment. b) Sample GDC-A2 after heat treatment at 1400°C. c) GDC-B3 after sintering at 1400°C. d) GDC-B4 after sintering at 1400°C.

Figure 3.3.a. shows the fracture surface of the sample GDC-A1 sintered at 1250°C. Its relative density after sintering was 88%. Figure 3.3.b. shows the same image of sample GDC-A2 which was sintered at 1400°C. The relative density of this sample after sintering was 94%. When these two samples are compared, it has been observed that the relative density increased as the final sintering temperature was raised. Figures 3.3.c and d. show fracture surfaces of infiltrated samples that were sintered at 1400°C. While

the porous scaffold had a density of 4.3 g/cm³. Its relative density after infiltration and sintering went up to 75% after 40x infiltration cycles and 74% after 50x infiltration cycles.

3.2. XRD and EDX Analysis Results

As received GDC powder was analyzed by XRD using CuK α radiation. The result is shown in Figure 3.4. As can be seen in Figure 3.4. the powder was crystalline and had only peaks for GDC with fluorite structure.

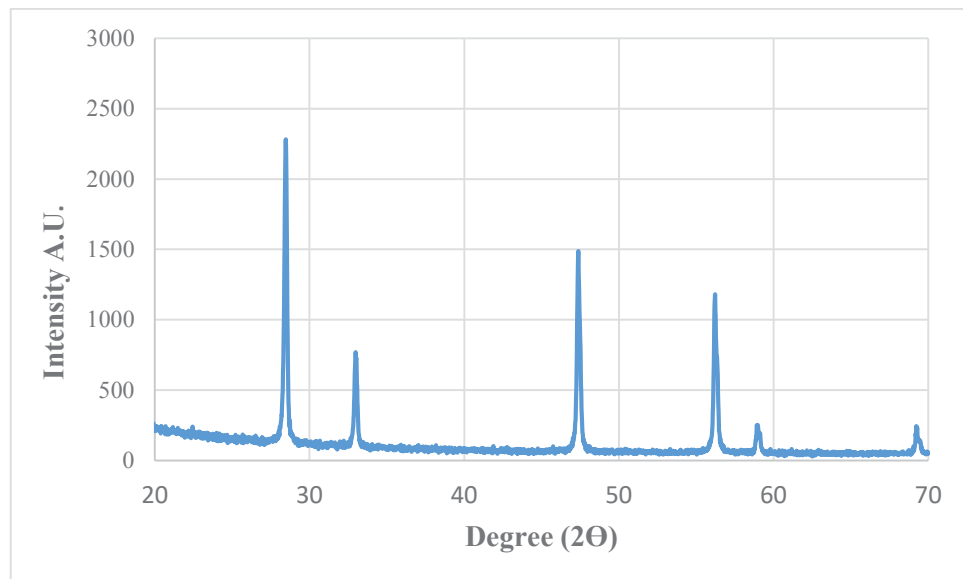


Figure 3. 4. XRD pattern of the prepared GDC powders. CuK α radiation was used. All peaks corresponded to GDC.

Figure 3.5 shows the energy dispersive X-Ray spectroscopy (EDX) analysis image of the GDC sample. As can be seen from the graph, GDC powder contains O, Ce and Gd elements. As seen in Table 3.1, elemental composition, atomic percentage and weight percentage of GDC powder were calculated using the quantitative EDS analysis method.

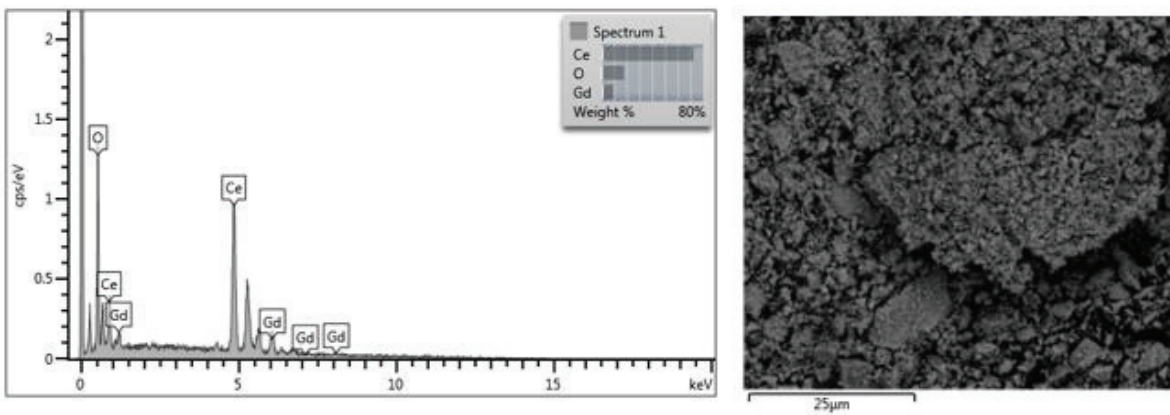


Figure 3.5. Energy dispersive X-Ray spectroscopy (EDX) analyses of GDC.

Table 3.1. Elemental composition as atomic percent and weight percent of GDC powder was determined by semi-quantitative EDS analysis.

Element	Wt%	Atomic %
O	17.96	66.00
Ce	72.50	30.43
Gd	9.55	3.57
Total:	100.00	100.00

3.3. Dilatometric Analyses

As explained above, four different samples were prepared for dilatometric analysis. A Linseis L75 vertical dilatometer was used for this purpose. Samples GDC-A1 and GDC-A2 were heated up to respectively 1250°C and 1400°C while the samples GDC-B3 and GDC-B4 were heated to 1400°C. Heating rates were kept constant in all runs at 3°C/min. Figure 3.6. shows the relative densification and densification rate curves for all pellets.

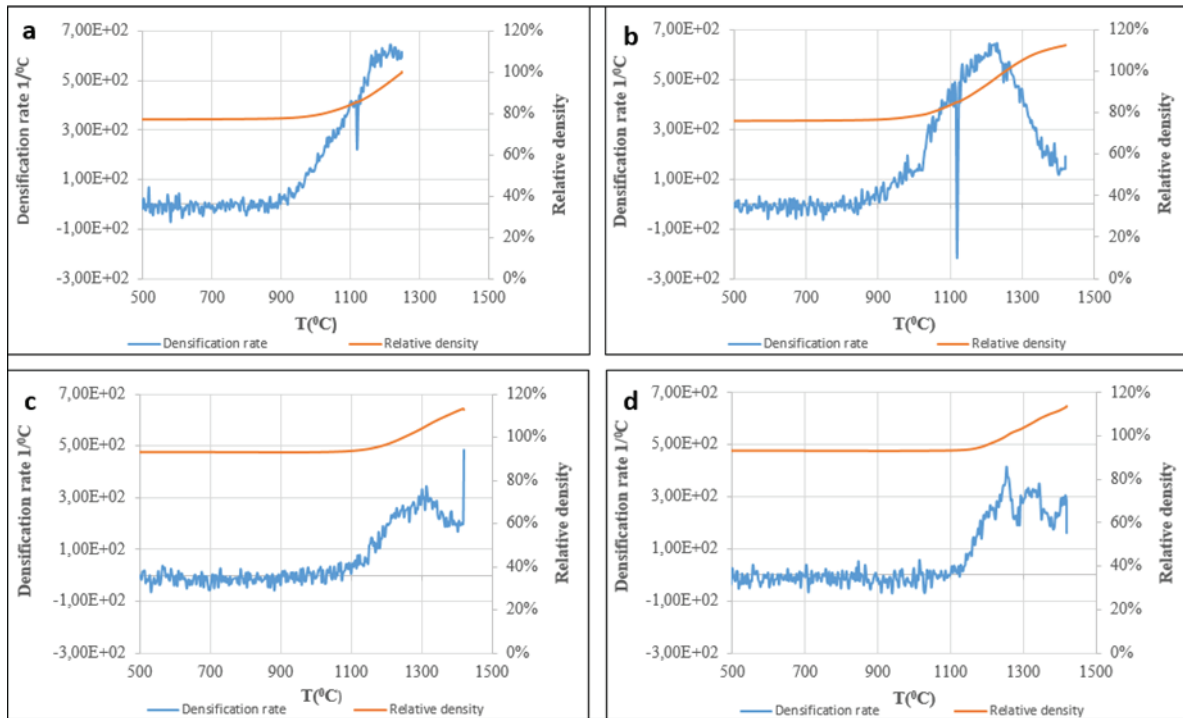


Figure 3.6. Relative density and densification rate as a function of temperature a) GDC-A1 b) GDC-A2 c) GDC-B3 and d) GDC-B4.

As can be seen in Figure 3.6.a and b samples GDC-A1 and GDC-A2 showed not much densification up until 900 °C at which point suddenly the particles started coalescence and shrinkage took place at a rapid rate reaching a maximum at 1200°C. Shrinkage and densification rates slowed down after this peak temperature. The dilatometer was not heated any further than 1250°C for GDC-A1 and 1400°C for GDC-A2 for fear of melting the pellet which may have jeopardized the push rod system. The infiltrated samples GDC-B3 and GDC-B4 were infiltrated 40 and 50 times, respectively. c) GDC-B3 sample was found to have not much appreciable densification until 1100°C at which temperature significant densification started to occur during heating. Maximum densification rate was observed around 1300°C for this sample. Surprisingly the nano particles placed inside the pores of the porous scaffold by infiltration did not help obtain densification at lower temperature. d) The GDC-B4 sample did not show much densification before 1120°C. The maximum densification rate was observed at 1340°C.

The main reason the densification temperature did not decrease was probably due to the fact that porous scaffold has already lost much of its surface area, the main driving force for sintering, before reaching these temperatures (i.e. $T>1000^{\circ}\text{C}$). Even if some

densification occurred around 500-1000°C in the precipitated nano particles situated in the pores of the scaffold this densification could not be recorded in the dilatometer and was not helpful in producing shrinkage of the overall pellet compact. All that these particles did was to constrict further shrinkage of the porous pellet. Table 3.2. shows the densities of the samples after dilatometer analysis.

Table 3. 2. Sintering temperatures and final densities of samples.

Code number	Compaction pressure (MPa)	Initial heat treatment (°C)	Final sintering with dilatometer (°C)	Final density (g/cc)	Relative density %
GDC-A1	340	—	1250	6.34	88
GDC-A2	340	—	1400	6.76	93
GDC-B3	340	1000	1400	5.39	75
GDC-B4	340	1000	1400	5.29	74

The variation of the linear shrinkage behavior of GDC samples with temperature is shown in Figures 3.7 (a-d). As can be seen in Figure 3.7a which shows the dilatometric curve of sample GDC-A1, there was no change in the sample from room temperature to 890°C. As the temperature was increased between 890-1100°C, GDC particles had significant thermally induced activity to reduce the surface area by forming bonds between the particles. This particle coalescence and shrinkage rate remained steady between 1100°C and 1250°C at which temperature the dilatometer was programmed to cool. This was the first sample tested, and the operator of the dilatometer was reluctant to test further to avoid premature meltdown of the pellet which might have stucked to the pushrod, the worst case that could happen in a dilatometer. In this temperature range neck formation occurred and total porosity decreased. As a result, a total linear shrinkage of up to 10% occurred in the pellet. There was no change in the sample during the gradual cooling from 1250°C to room temperature. GDC-A2 sample showed a similar behavior with the only difference that the latter was heated up to a temperature of 1400°C. Sample GDC-B3 showed a similar pattern during heating but showed an accelerated sintering beginning from 1060°C. Between 1060°C and 1400°C distance between particles decreased, necks grew, porosity decreased, shrinkage occurred in the material. Total

linear shrinkage of the sample was about 8%. Sample GDC-B4 did not change from room temperature to 1130°C. This meant a late sintering activity of the infiltrated scaffold.

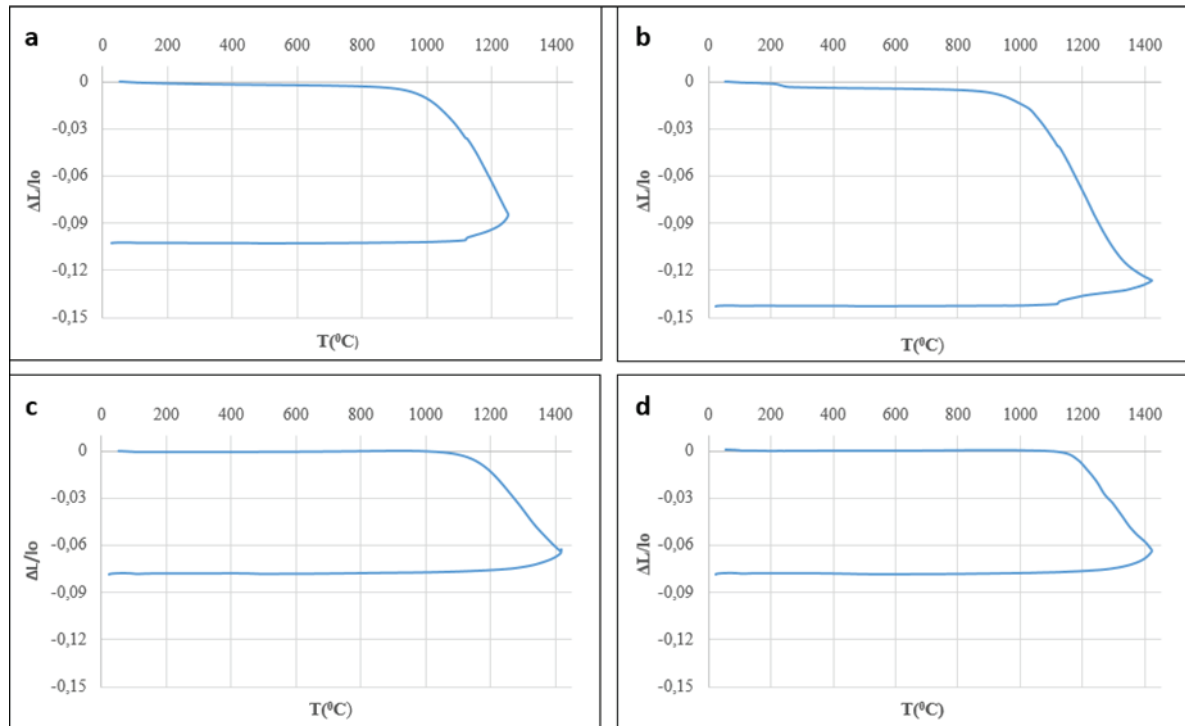


Figure 3. 7. The variation of the linear shrinkage behavior of the GDC samples with temperature. a) GDC-A1, b) GDC-A2, c) GDC-B3 and d) GDC-B4.

The relative shrinkage and shrinkage rate behaviors of GDC pellets are shown in Figures 3.8 and 3.9. As can be seen in both Figure 3.8 and 3.9, sample GDC-A2 begins to densify around 910°C and begins to shrink considerably until the highest heating temperature of 1400°C. The maximum shrinkage rate occurred around 1125°C. GDC-B3 and GDC-B4 samples initially showed an expansion tendency with the effect of temperature. This was probably due to the porous scaffold structure which was presintered at 1000°C. Samples GDC-B3 and B4 behaved similarly and started to densify around 1060°C with a maximum shrinkage rate seen around 1240°C. The main difference between these 3 samples (untreated GDC-A2, 40 times infiltrated GDC-B3 and 50 times infiltrated GDC-4), which are heat treated up to a maximum of 1400°C, is that the increase in the infiltrating process caused the densification temperature to be delayed. This was a

surprising finding as explained above. Our explanation is that nanoparticles in the pores sinter very early and delay shrinkage.

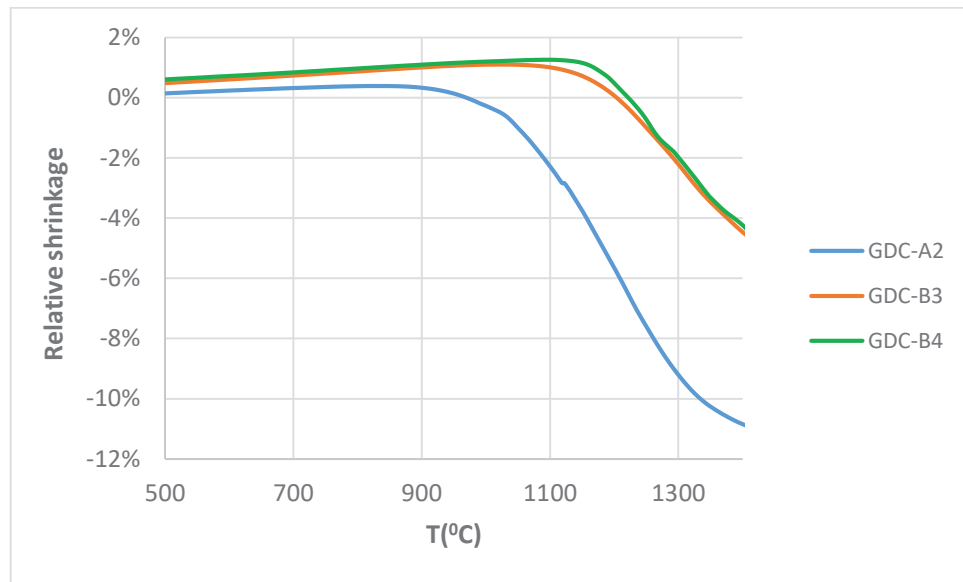


Figure 3. 8. Relative shrinkage curves of infiltrated and non-infiltrated GDC pellets sintered at 1400°C in different cycles.

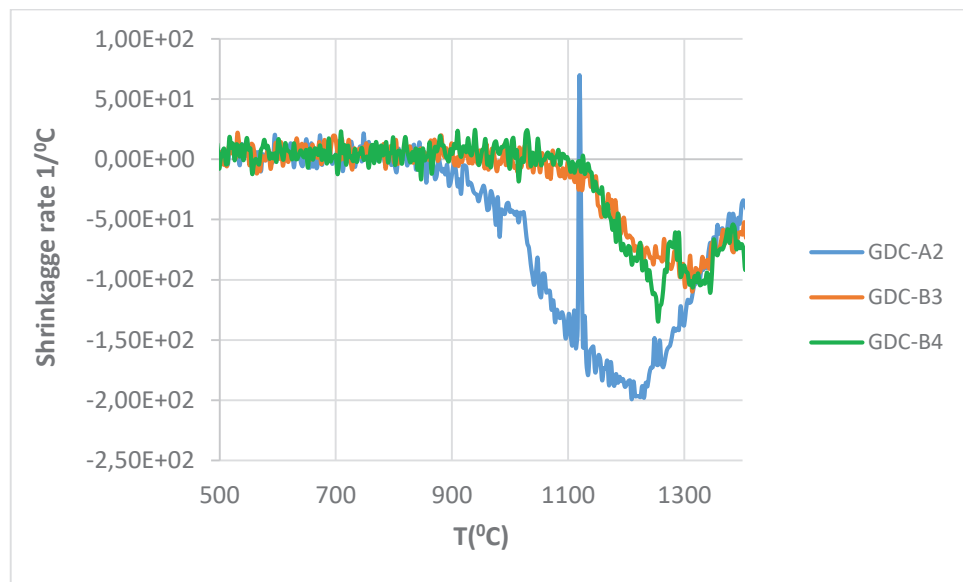


Figure 3. 9. Shrinkage rate curves of infiltrated and non-infiltrated GDC pellets sintered at 1400°C in different cycles.

Nano GDC particles placed in the pores by infiltration was expected to help the GDC pellet to densify earlier. According to our expectations, the same infiltrated GDC scaffold samples were expected to begin densification at approximately 700°C, perhaps even lower depending on the surface area of the nanoparticles in the pores. However, these experiments did not turn out as we expected. Contrary to what we expected, the densification temperature increased. The main reason for this is that the polymeric GDC solution coated the outer surface of the porous scaffold like a film. This is schematically shown in Figure 3.10.

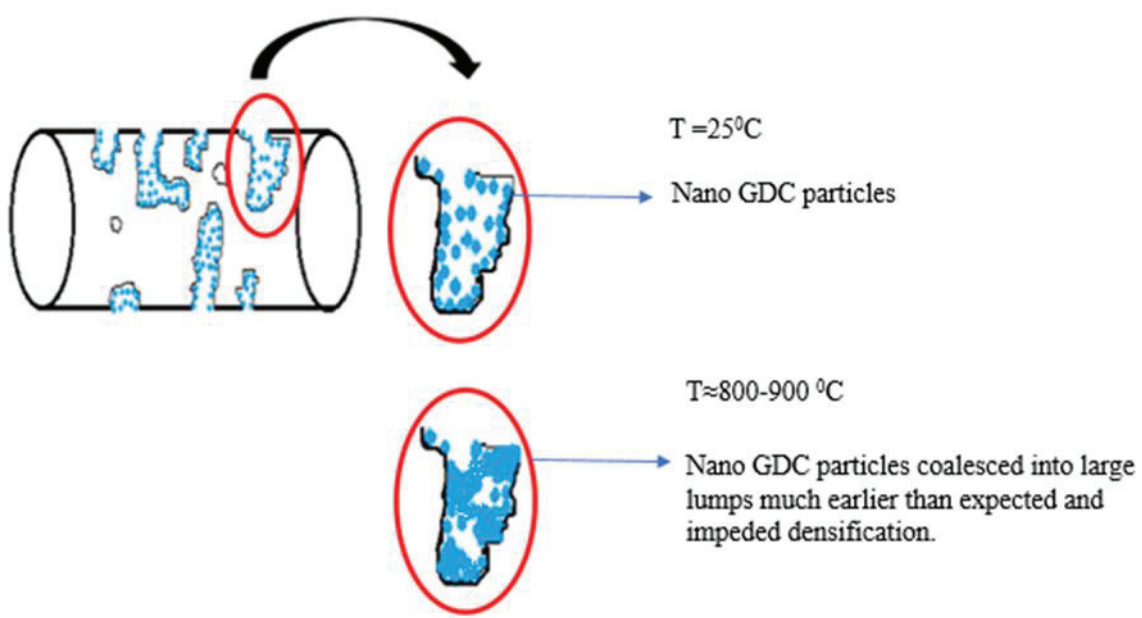


Figure 3. 10. Demonstration of particle growth in the porous structure of nano GDC powder at room temperature and nano GDC powders fired at 800-900°C.

While most researchers have used $\text{Ce}_{0.9}\text{Gd}_{0.1}\text{O}_{1.9}$ (a GDC doped with Gd 10mol% doped), Nicollet et al. conducted their studies to densify the powder compact (pellet) using 20% Gd doped ceria ($\text{Ce}_{0.8}\text{Gd}_{0.2}\text{O}_{1.9}$). Li, Cu and Zn nitrates were added to the GDC powders by infiltration method to obtain a more dense structure. It was hoped that these additions could accelerate the densification process. Indeed, they have successfully reduced the densification temperature of the material with the help of the infiltration technique. For example, while the sintering temperature of pure GDC was 1330°C, this temperature was decreased to 1080°C with the incorporation of a 3% Li mixture via

infiltration. When their densities are to be compared, Li led to 95% density at 1000°C, and the mixture containing Zn required 1250°C for a relative density of 90%. It is known that 1450°C are needed for pure GDC to reach the same density (Nicollet et al. 2017).

Sistla et al., studied the densification and grain growth kinetics of gadolinium doped (10 mol%) Ce(GDC10) during sintering by isothermal sintering experiments. GDC, which had a density of 50% at the beginning, reached a density of 94% at 1400°C sintering capacity. They noted that GDC10 powder started to densify at 800°C. It was recorded that it reaches the maximum densification of 1075°C. (Sistla et al. 2020).

Prasad et al., worked with nanocrystalline GDC powders to achieve high sinterability at low temperatures using the glycine nitrate process (GNP). The effect of glycine content on particle size, morphology and sintering behavior was investigated by changing the glycine-nitrate (G/N) ratio ($0.1 \leq 0.3 \leq 0.55$) during combustion synthesis. As a result of this work; they found that a G/N ratio of 0.55 is the best condition to obtain GDC powders with smaller particle sizes and of very high quality. With this mixing ratio, the sintering temperature is 1200°C and the relative density is 97% (Prasad et al. 2010b).

Cheng et al. used the gel-casting method to create the single-phase fluorite structure of nanoscale $\text{Ce}_{0.9}\text{Gd}_{0.1}\text{O}_{1.95}$ (gadolinia doped ceria, GDC). In their study, they examined the sintering behavior and ionic conductivity of the powders with increasing temperature from 600°C to 1000°C. They noted that the densities of the samples prepared from the powders calcined at different temperatures at 600°C, 800°C and 1000°C after sintering at 1500°C for 5 hours were 98.4%, 97.5% and 96.1%, respectively. They observed that the density and ionic conductivity increased with the temperature (Cheng et al. 2003).

Figure 3.11. shows the result of the SEM analysis of the GDC-B4. Figure 3.11.a, b respectively are the porous inner surface and dense outer surface of GDC-B4 after 50 times infiltration.

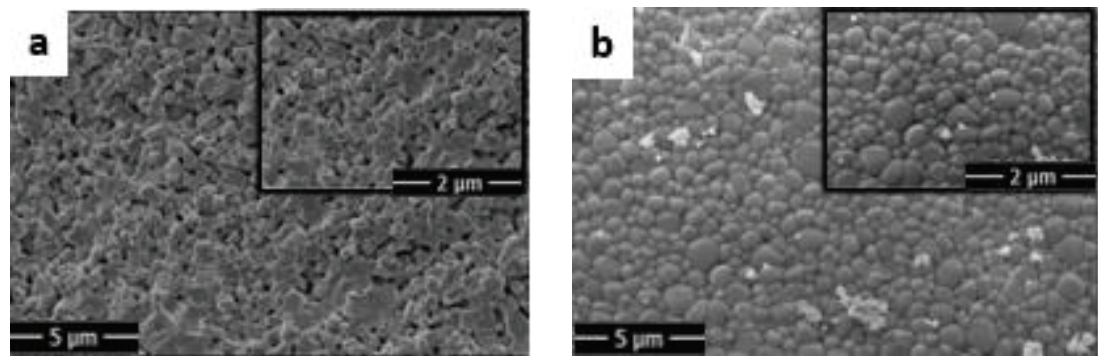


Figure 3. 11. a) Inner surface b) outer surface of infiltrated porous scaffold.

The surface area of the pellets exposed to the heating surface on hot plate, was larger in Sındıracı et al. study than that of the pellets in this study (Figure 3.12.a). Pellets with larger exposed surface area were naturally heated more effectively. Hence this allowed the infiltration solvent to evaporate faster in thin pellets of Sındıracı study. Because the exposed surface area of the pellets used in this study was smaller, they were exposed to less effective heating and the evaporation process took place more slowly (Figure 3.12.b). Re-infiltration without complete evaporation resulted in the formation of prematurely densified layers on the surface. This can be seen clearly in Figures 3.11b and 3.13b.

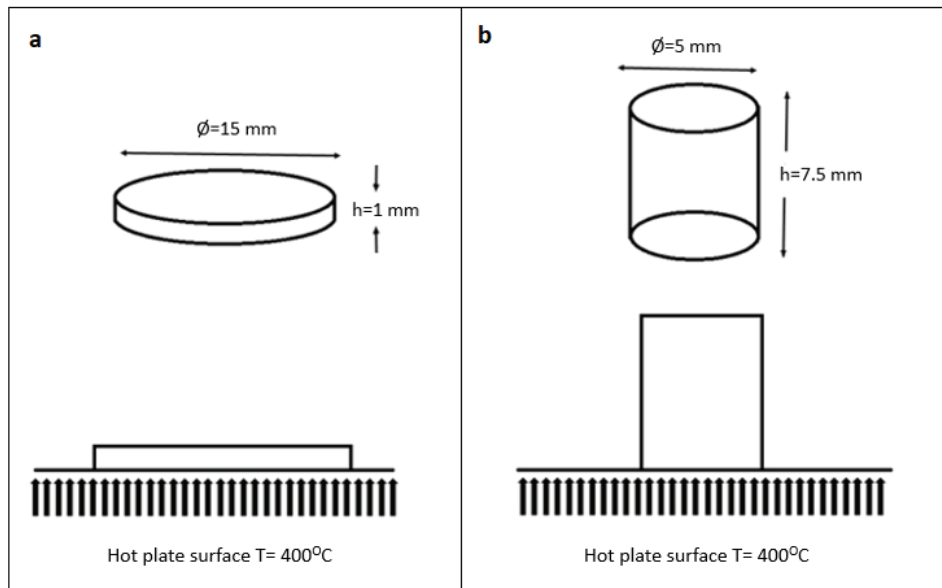


Figure 3. 12. a) The pellet used by Sındıracı et al., b) the pellet used in this study.

Figure 3.13.a. shows a fractured specimen, the inner surface of which was matte and porous. Figure 3.13.b shows a glossy surface on the outer side of the same pellet, suggesting the formation of a dense layer on the outside.



Figure 3. 13. a) Matt interior b) glossy exterior of infiltrated porous scaffold.

CHAPTER 4

CONCLUSION

The electrolyte, which is a component of solid oxide fuel cells, is desired to have a dense structure. The desired relative density should be greater than 95%. The reason for this is to avoid a possible gas leak or short circuit during the operation of the SOFC. Ceramic materials used in making electrolytes are generally densified by sintering at high temperatures. In this study, it is aimed to decrease the densification temperature of the electrolyte material to save on the cost of processing as lower sintering temperature means less furnace time and energy consumption. In this way, electrolytes can be produced easily and at a lower cost. GDC is generally used as the electrolyte material in SOFCs. GDC needs high temperatures (approximately 1400-1500°C) in order to reach the desired density. In this study; experimentally, it is aimed to densify GDC material at lower temperatures, approximately 1200°C. Infiltration technique has been used to achieve the desired density at lower temperatures. In order to realize the density increase, porous scaffolds of GDC were infiltrated by a number of cycles (40 or 50 times). So follow the experimental steps more easily, two different experimental groups were formed. Pellets were compressed under 340 MPa pressure to be used in both experimental groups. First sample group was directly sintered in a vertical dilatometer at different temperatures. The infiltrated group was first sintered at 1000°C to form a porous GDC scaffold. It was then infiltrated with a different number of cycles. Multiple infiltration and drying cycles were intended to fill the pores with GDC nanoparticles, which are expected to help densification at lower temperatures. Two different groups, infiltration and non-infiltration, were formed and their temperature and infiltration cycles and densification behavior were examined using a vertical dilatometer. The porous GDC scaffold was infiltrated with a polymeric solution prepared from $\text{Ce}(\text{NO}_3)_{3.6}\text{H}_2\text{O}$ and $\text{Gd}(\text{NO}_3)_{3.6}\text{H}_2\text{O}$. The prepared samples were sintered at 1400°C. As a result of the experiments, it was observed that the densification increased with the increase of temperature and decreased with infiltration cycles. This is thought to be because the porous scaffold could not be completely dried during the infiltration cycles. This led to the formation of a dense outer

layer of GDC and a porous inner layer. This dense outer layer prevented shrinkage of the pellet during dilatometric analysis. Further studies are required for complete evaporation of the solvent during drying of the filtered pellets.

REFERENCES

- Abdalla, Abdalla M., Shahzad Hossain, Atia T. Azad, Pg Mohammad I. Petra, Feroza Begum, Sten G. Eriksson, and Abul K. Azad. 2018. “Nanomaterials for Solid Oxide Fuel Cells: A Review.” *Renewable and Sustainable Energy Reviews* 82 (August 2017): 353–68. <https://doi.org/10.1016/j.rser.2017.09.046>.
- ASTM International. 2000. “Standard Test Methods for Apparent Porosity, Water Absorption, Apparent Specific Gravity, and Bulk Density of Burned Refractory Brick and Shapes by Boiling Water (ASTM C20-00).” *ASTM International, West Conshohocken, PA*, no. July: 3. <https://doi.org/10.1520/C0020-00>.
- Baharuddin, Nurul Akidah, Andanastuti Muchtar, and Mahendra Rao Somalu. 2017. “Short Review on Cobalt-Free Cathodes for Solid Oxide Fuel Cells.” *International Journal of Hydrogen Energy* 42 (14): 9149–55. <https://doi.org/10.1016/j.ijhydene.2016.04.097>.
- Buyukaksoy, Aligul, and Viola I. Birss. 2016. “Highly Active Nanoscale Ni - Yttria Stabilized Zirconia Anodes for Micro-Solid Oxide Fuel Cell Applications.” *Journal of Power Sources* 307: 449–53. <https://doi.org/10.1016/j.jpowsour.2015.12.022>.
- Caisso, Marie, Rémy Boulesteix, Sébastien Picart, Alexandre Maître, Thibaud Delahaye, and André Ayral. 2017. “Investigation of the Sintering Mechanisms of GDC Pellets Obtained by the Compaction of Nanostructured Oxide Microspheres.” *Journal of the American Ceramic Society* 100 (10): 4450–60. <https://doi.org/10.1111/jace.14993>.
- Chen, C C, M M Nasrallah, and H U Anderson. 1994. “/ HOMOGENEOULLOLUTLO” 71: 101–8.
- Cheng, Ji Gui, Shao Wu Zha, Jia Huang, Xing Qin Liu, and Guang Yao Meng. 2003. “Sintering Behavior and Electrical Conductivity of Ce_{0.9}Gd_{0.1}O_{1.95} Powder Prepared by the Gel-Casting Process.” *Materials Chemistry and Physics* 78 (3): 791–95. [https://doi.org/10.1016/S0254-0584\(02\)00384-X](https://doi.org/10.1016/S0254-0584(02)00384-X).
- Dwivedi, Sudhanshu. 2019. “ScienceDirect Solid Oxide Fuel Cell : Materials for Anode , Cathode and Electrolyte.” *International Journal of Hydrogen Energy*, no. xxxx.

- https://doi.org/10.1016/j.ijhydene.2019.11.234.
- . 2020. “Solid Oxide Fuel Cell: Materials for Anode, Cathode and Electrolyte.” *International Journal of Hydrogen Energy* 45 (44): 23988–13. https://doi.org/10.1016/j.ijhydene.2019.11.234.
- Giorgi, Leonardo. 2013. “Fuel Cells: Technologies and Applications.” *The Open Fuel Cells Journal* 6 (1): 0–0. https://doi.org/10.2174/1875932720130719001.
- Giorgi, Leonardo, and Fabio Leccese. 2013. “Fuel Cells: Technologies and Applications,” 1–20.
- Hoogers, Gregor. 2002. *Fuel Cell Technology Handbook*. *Fuel Cell Technology Handbook*. https://doi.org/10.5860/choice.40-6435.
- Huang, Kevin, and John B. Goodenough. 2009a. “Electronic Properties of Solids for Solid Oxide Fuel Cells (SOFCs).” *Solid Oxide Fuel Cell Technology*, 23–40. https://doi.org/10.1533/9781845696511.23.
- . 2009b. “Materials for Solid Oxide Fuel Cells (SOFCs).” *Solid Oxide Fuel Cell Technology*, 220–68. https://doi.org/10.1533/9781845696511.220.
- Hunkel, Martin, Holger Surm, and Matthias Steinbacher. 2018. “Dilatometry.” *Handbook of Thermal Analysis and Calorimetry* 6: 103–29. https://doi.org/10.1016/B978-0-444-64062-8.00019-X.
- Irshad, Muneeb, Khurram Siraj, Rizwan Raza, Anwar Ali, Pankaj Tiwari, Bin Zhu, Asia Rafique, Amjad Ali, Muhammad Kaleem Ullah, and Arslan Usman. 2016. “A Brief Description of High Temperature Solid Oxide Fuel Cell’s Operation, Materials, Design, Fabrication Technologies and Performance.” *Applied Sciences (Switzerland)* 6 (3). https://doi.org/10.3390/app6030075.
- Ishihara, Tatsurni, Nigel M. Sammes, and Osamu Yamamoto. 2003. “Electrolytes.” *High-Temperature Solid Oxide Fuel Cells: Fundamentals, Design and Applications*, 83–117. https://doi.org/10.1016/B978-185617387-2/50021-0.
- Jamil, Zadariana, Enrique Ruiz-Trejo, Paul Boldrin, and Nigel P. Brandon. 2016. “Anode Fabrication for Solid Oxide Fuel Cells: Electroless and Electrodeposition of Nickel and Silver into Doped Ceria Scaffolds.” *International Journal of Hydrogen Energy* 41 (22): 9627–37. https://doi.org/10.1016/j.ijhydene.2016.04.061.

- Kang, S-J.L. 2010. *Liquid Phase Sintering. Sintering of Advanced Materials*. Woodhead Publishing Limited. <https://doi.org/10.1533/9781845699949.1.110>.
- Kaur, Mandeep, Gurbinder Kaur, and V. Kumar. 2020. *Understanding Intermediate Temperature Solid Oxide Fuel Cells. Intermediate Temperature Solid Oxide Fuel Cells*. INC. <https://doi.org/10.1016/b978-0-12-817445-6.00001-6>.
- Kaur, Paramvir, and K. Singh. 2020a. “Review of Perovskite-Structure Related Cathode Materials for Solid Oxide Fuel Cells.” *Ceramics International* 46 (5): 5521–35. <https://doi.org/10.1016/j.ceramint.2019.11.066>.
- Kaur, Paramvir, and K Singh. 2020b. “Review of Perovskite-Structure Related Cathode Materials for Solid Oxide Fuel Cells.” *Ceramics International* 46 (5): 5521–35. <https://doi.org/10.1016/j.ceramint.2019.11.066>.
- Kilner, J. A., J. Druce, and T. Ishihara. 2016. *Electrolytes. High-Temperature Solid Oxide Fuel Cells for the 21st Century: Fundamentals, Design and Applications: Second Edition*. <https://doi.org/10.1016/B978-0-12-410453-2.00004-X>.
- Kingery, W. David, H.K. Bowen, and Donald R. Uhlmann. 1976. *Introduction to Ceramics (2nd Edition)*. John Wiley & Sons, Inc.
- Kumar, Abhishek. 2008. “TP3 - Ceramics : Sintering and Microstructure.” *Ceramics & Colloids*, 1–15.
- Leng, Yongjun, Siew Hwa Chan, and Qinglin Liu. 2008. “Development of LSCF-GDC Composite Cathodes for Low-Temperature Solid Oxide Fuel Cells with Thin Film GDC Electrolyte.” *International Journal of Hydrogen Energy* 33 (14): 3808–17. <https://doi.org/10.1016/j.ijhydene.2008.04.034>.
- Machrafi, Hatim. 2012. *Green Energy and Technology. Green Energy and Technology*. <https://doi.org/10.2174/97816080528511120101>.
- Mench, Matthew M. 2006. “Fuel Cells.” *Mechanical Engineers’ Handbook: Energy and Power: Third Edition* 4: 922–57. <https://doi.org/10.1002/0471777471.ch28>.
- Milewski, J, and J Lewandowski. 2010. “Analysis of Design and Construction of Solid Oxide Fuel Cell in Terms of Their Dynamic Operation.” *Archivum Combustionis* 30 (3): 145–54.
- Minh, Nguyen Quang, and Takehiko Takahashi. 1995. “Introduction.” *Science and*

Technology of Ceramic Fuel Cells, no. iii: 1–14. <https://doi.org/10.1016/b978-044489568-4/50002-5>.

- Nicollet, Clement, Jenny Waxin, Thomas Dupeyron, Aurélien Flura, Jean Marc Heintz, Jan Pieter Ouweltjes, Paolo Piccardo, Aline Rougier, Jean Claude Grenier, and Jean Marc Bassat. 2017. “Gadolinium Doped Ceria Interlayers for Solid Oxide Fuel Cells Cathodes: Enhanced Reactivity with Sintering Aids (Li, Cu, Zn), and Improved Densification by Infiltration.” *Journal of Power Sources* 372 (December 2017): 157–65. <https://doi.org/10.1016/j.jpowsour.2017.10.064>.
- Prasad, Dasari Hari, Ji Won Son, Byung Kook Kim, Hae Weon Lee, and Jong Ho Lee. 2010a. “A Significant Enhancement in Sintering Activity of Nanocrystalline Ce_{0.9}Gd_{0.1}O_{1.95} Powder Synthesized by a Glycine-Nitrate-Process.” *Journal of Ceramic Processing Research* 11 (2): 176–83.
- . 2010b. “A Significant Enhancement in Sintering Activity of Nanocrystalline Ce_{0.9}Gd_{0.1}O_{1.95} Powder Synthesized by a Glycine-Nitrate-Process.” *Journal of Ceramic Processing Research* 11 (2): 176–83. <https://doi.org/10.36410/jcpr.2010.11.2.176>.
- Rahaman, M.N. 2010. “Kinetics and Mechanisms of Densification.” *Sintering of Advanced Materials*, 33–64. <https://doi.org/10.1533/9781845699949.1.33>.
- Rahaman, Mohamed N. 1989. *Science of Sintering Ceramic Matrix Composites. Processing of Ceramic and Metal Matrix Composites*. The Canadian Institute of Mining and Metallurgy. <https://doi.org/10.1016/b978-0-08-037298-3.50012-8>.
- Sarfraz, Amina, Asif Hassan Raza, Mojtaba Mirzaeian, Qaisar Abbas, and Rizwan Raza. 2020. “Electrode Materials for Fuel Cells.” *Reference Module in Materials Science and Materials Engineering*, 1–16. <https://doi.org/10.1016/b978-0-12-803581-8.11742-4>.
- Shao, Zongping, and Moses O. Tadé. 2016a. *Cathodes for IT-SOFCs*. https://doi.org/10.1007/978-3-662-52936-2_3.
- Shao, Zongping, and Moses O Tadé. 2016b. *Green Chemistry and Sustainable Technology Intermediate- Temperature Solid Oxide Fuel Cells Materials and Applications. Intermediate-Temperature Solid Oxide Fuel Cells*. <https://doi.org/10.1007/978-3-662-52936-2>.

Sharifzadeh, Mahdi, Wenqian Chen, Giorgio Triulzi, Mirko Hu, Tohid N. Borhani, Majid Saidi, Venkatesan Krishnan, et al. 2020. *Design and Operation of Solid Oxide Fuel Cell Systems: Challenges and Future Research Directions. Design and Operation of Solid Oxide Fuel Cells*. Elsevier Inc. <https://doi.org/10.1016/b978-0-12-815253-9.00015-x>.

Sistla, S. K., T. Mishra, Y. Deng, A. Kaletsch, M. Bram, and C. Broeckmann. 2020. “Electric Field-Assisted Sintering of Gadolinium-Doped Ceria: Sintering and Grain Growth Kinetics.” *Journal of Ceramic Science and Technology* 11 (1): 17–25. <https://doi.org/10.4416/JCST2019-00045>.

Sındıraç, Can, Aligül Büyükkaksoy, and S. Akkurt. 2019. “Electrical Properties of Gadolinia Doped Ceria Electrolytes Fabricated by Infiltration Aided Sintering.” *Solid State Ionics* 340 (July). <https://doi.org/10.1016/j.ssi.2019.115020>.

Sındıraç, Can, Seda Çakırlar, Aligül Büyükkaksoy, and Sedat Akkurt. 2019. “Lowering the Sintering Temperature of Solid Oxide Fuel Cell Electrolytes by Infiltration.” *Journal of the European Ceramic Society* 39 (2–3): 409–17. <https://doi.org/10.1016/j.jeurceramsoc.2018.09.029>.

Sundén, Bengt. 2019. “Fuel Cell Types - Overview.” *Hydrogen, Batteries and Fuel Cells*, 123–44. <https://doi.org/10.1016/b978-0-12-816950-6.00008-7>.

Tarancón, Albert. 2009. “Strategies for Lowering Solid Oxide Fuel Cells Operating Temperature.” *Energies* 2 (4): 1130–50. <https://doi.org/10.3390/en20401130>.

Viswanathan, Balasubramanian. 2016. *Energy Sources: Fundamentals of Chemical Conversion Processes and Applications. Energy Sources: Fundamentals of Chemical Conversion Processes and Applications*.

Weber, André, and Ellen Ivers-Tiffée. 2004. “Materials and Concepts for Solid Oxide Fuel Cells (SOFCs) in Stationary and Mobile Applications.” *Journal of Power Sources* 127 (1–2): 273–83. <https://doi.org/10.1016/j.jpowsour.2003.09.024>.

Xu, Xu. 2018. “Ceramics in Solid Oxide Fuel Cells for Energy Generation.” *Advances in Ceramic Matrix Composites: Second Edition*, 763–88. <https://doi.org/10.1016/B978-0-08-102166-8.00031-1>.

Yalamaç, Emre. 2010. “Sintering, Co-Sintering and Microstructure Control of Oxide Based Materials: Zirconia, Alumina, Spinel, Alumina-Zirconia and Spinel-

Alumina,” no. June.

- Zhu, W. Z., and S. C. Deevi. 2003. “A Review on the Status of Anode Materials for Solid Oxide Fuel Cells.” *Materials Science and Engineering A* 362 (1–2): 228–39.
[https://doi.org/10.1016/S0921-5093\(03\)00620-8](https://doi.org/10.1016/S0921-5093(03)00620-8).